



# Lithium-ion battery physics and statistics-based state of health model

Alasdair J. Crawford<sup>a,\*</sup>, Daiwon Choi<sup>a</sup>, Patrick J. Balducci<sup>b</sup>, Venkat R. Subramanian<sup>c</sup>,  
Vilayanur V. Viswanathan<sup>a,\*\*</sup>

<sup>a</sup> Energy & Environment Division, Pacific Northwest National Laboratory, P.O. Box 999, Richland, WA, 99352, USA

<sup>b</sup> Energy Systems Division, Argonne National Laboratory, Lemont, IL, 60439, USA

<sup>c</sup> Walker Department of Mechanical Engineering & Material Science Engineering, Texas Materials Institute, The University of Texas at Austin, Austin, TX, 78712, USA

## HIGHLIGHTS

- Physics-based pseudo-2d model simulates performance degradation of Li-ion batteries.
- Multiple degradation phenomena modeled, including their interactions.
- Missing parameter values from literature estimated from global fit to data.
- 0d model approximation better estimates key differentiating degradation parameters.
- Physics-based model informs statistics-based model predicting degradation.

## ARTICLE INFO

### Keywords:

Battery  
Health  
Degradation  
Solid electrolyte interphase  
Diffusion  
Dissolution

## ABSTRACT

A pseudo-2d model using COMSOL Multiphysics® software simulates performance degradation of Li-ion batteries when subjected to peak shaving grid service. Multiple degradation pathways are considered, including solid electrolyte interphase (SEI) formation and breakdown, cathode dissolution and its effect on SEI formation. The model is validated by simulating commercial cell performance. We develop a global model simulating performance across all chemistries, along with a model treating chemistries individually. There is good agreement between these two models for various optimization parameters such as SEI equilibrium potential, cathode dissolution exchange current density, solvent diffusivity in the SEI and SEI ionic conductivity. To circumvent time constraints related to the COMSOL model, a 0d global model is developed, which fits data well. Good agreement for various optimization parameters is obtained among the COMSOL global & individual chemistry models and the 0-d model. A top-down, statistics-based model using current, voltage, and anode expansion rate as degradation predictors is developed using insights from the physics-based model. This model predicts degradation for multiple grid services and electric vehicle drive cycles with high accuracy and provides the pathway to develop an efficient battery management system combining machine learning and findings from computationally intensive physics-based algorithms.

## 1. Introduction

Lithium-ion batteries degrade over time due to multiple mechanisms including loss of lithium, loss of active material or increase in internal resistance. This work models battery degradation using a multifaceted approach. A physics-based bottom-up approach models various physical phenomena, associated degradation mechanisms, and their interactions.

Also, a statistical approach incorporating learnings from the physics-based model uses regression methods to predict capacity loss. Both approaches are validated using in-house single cell data.

Lithium-ion battery models fall in the following categories:

- Empirical
- Single Particle

\* Corresponding author.

\*\* Corresponding author.

E-mail addresses: [Alasdair.crawford@pnnl.gov](mailto:Alasdair.crawford@pnnl.gov) (A.J. Crawford), [Daiwon.choi@pnnl.gov](mailto:Daiwon.choi@pnnl.gov) (D. Choi), [pbalducci@anl.gov](mailto:pbalducci@anl.gov) (P.J. Balducci), [venkat.subramanian@utexas.edu](mailto:venkat.subramanian@utexas.edu) (V.R. Subramanian), [Vilayanur.viswanathan@pnnl.gov](mailto:Vilayanur.viswanathan@pnnl.gov) (V.V. Viswanathan).

<https://doi.org/10.1016/j.jpowsour.2021.230032>

Received 22 February 2021; Received in revised form 21 April 2021; Accepted 10 May 2021

0378-7753/© 2021 Published by Elsevier B.V.

- Pseudo 2-d
- 3-d

The original work in this area was from Newman's team on aqueous batteries [1–3]. The principles outlined have remained in place and are used for modeling lithium-ion chemistry performance and its degradation [4]. Building on this work, multiple groups have looked at various aspects of li-ion battery degradation such as solid electrolyte interphase (SEI) formation [5,6], cathode dissolution [6], lithium plating [7,8] and active material loss due to repeated stress during cycling [9,10]. To the best of our knowledge, no single work considers all these phenomena. More importantly, the interaction of one phenomenon with another, such as active material dissolution on SEI growth, has not been investigated in the literature. We attempt to consider all these degradation phenomena and their interactions.

Battery capacity decreases in five ways [11]:

- Loss of lithium due to SEI build-up at the negative
- Loss of lithium due to plating at the negative electrode
- Loss of active material at the negative
- Loss of lithium due to SEI build-up at the positive
- Loss of active material at the positive

In this work, lithium loss via SEI build-up in the cathode has not been considered, since the upper voltage limit during charge was restricted for the peak shaving duty cycle as discussed later. Lithium loss due to plating at the negative is also not considered, since the negative electrode potential is not expected to approach the plating region for the operating regimes considered in this work. Lithium loss at the negative electrode can be related to SEI growth during rest and operation, and stability of the SEI [12]. SEI growth rate has been modeled assuming electron tunneling as the electron source for SEI formation [13], assuming the SEI layer peels off during discharge, and SEI layer formation on the freshly exposed graphite surface during charge. In this work, the SEI is assumed to be an electronic insulator, with its growth rate determined by the SEI formation kinetics represented by the Butler-Volmer equation [12] at the graphite-SEI interface, and limited by solvent diffusion through the SEI [14].

Ramadass et al. [15] and Awarke et al. [16] used the Butler Volmer reaction to estimate SEI formation rate without accounting for ohmic drop across the SEI layer for both charge transfer and SEI formation. However, lithium ions diffuse through the SEI layer for both the desired intercalation at the electrode and SEI formation. Hence in this work, the overpotential for both reactions is reduced by the ohmic drop through the SEI layer [6].

In other work, the solvent diffusivity in the SEI varied with C rate [17]. This was because the magnitude of current was used as a proxy for particle cracking due to stress, incorporating particle cracking and SEI layer cracking into one reaction. In this work, particle cracking and SEI cracking are modeled as separate reactions, and exposure of the underlying fresh graphite surface for SEI formation is modeled by removing the solvent diffusion limitation.

For SEI exchange current density, three orders of magnitude difference were reported [6,18]. Fu et al. [18] overestimated exchange current density for SEI formation by assigning self-discharge losses to SEI layer formation. Using a lower equilibrium potential for SEI formation resulted in a further overestimation of exchange current density. In this work, a geometric mean of the reported exchange current density from both groups is used as the initial estimate, and then optimized to fit the data.

Laresgoiti [19] investigated SEI layer fracture to determine the SEI growth rate on freshly exposed exposure graphite. Tangential stress at the SEI layer was estimated and compared with the SEI yield strength. However, due to a lack of reliable data on SEI yield stress, it was found that even for a  $\Delta z$  as low as 0.01 in  $\text{Li}_2\text{C}_6$ , the estimated tangential stress was greater than the SEI yield strength, resulting in all SEI fracturing

during discharge, followed by the formation of fresh SEI on the freshly exposed graphite surface. However, for li-ion batteries with a graphite anode, the SEI layer is quite stable and not readily susceptible to fracture [20]. Hence our work uses the graphite volumetric change per mole lithium intercalated data [3], along with the empirical relationship proposed by Kinderman [6] to evaluate SEI fracture as a function of current.

Dissolution of layered cathodes has been explored in earlier work [6]. To explain the difference in degradation between lithium-ion batteries with different cathode chemistries, we include an interaction between the SEI layer formation reaction and dissolved Ni from the cathode [21–23].

Negative and positive active material loss occurs due to stress related cumulative fatigue that exceeds the material yield stress [10], resulting in that portion of the active material being isolated from the rest of the electrode. The impact of repeated stresses on the particle is determined by using the fatigue criterion for the active material. The ratio of the surface stress to its yield stress is used as a proxy for fatigue [10], with a probability of failure as a function of this ratio obtained from the literature [24].

Battery energy storage system (BESS) state of health (SOH) prediction under various operating regimes is a valuable input to economic models used for BESS deployment. This prediction algorithm may either reside within the BESS or may be integrated within the economic model. In either case, the SOH model is unlikely to be doing complicated, computationally intensive physics modeling. Instead, it is more likely to be statistical or machine learning based modeling, where the battery's history predicts its future performance. Statistical models can also give high level insights into overall trends [25]. Hence, developing a statistical model is an important aspect of SOH modeling.

However, this does not make the physics-based models unimportant. Reliable statistical models require good insight into the underlying phenomena. The better we understand the physics of battery degradation, the better a statistical model we can develop, by understanding what interactions are important and how we should transform input variables to the statistical model. In the top-down model section, we bring insights from the physics-based models into the statistical model. The capacity degradation is predicted for each capacity test, while only training on data from previous tests. This ensures the model's predictive capability is evaluated. Another important aspect of physics-based models is their application to safety, as there is coupling between the heat generated and the chemical reactions [26]. Physics-based models can be used to estimate heat generation rates from interactions between the electrolyte and anode/cathode at various states of charge and operating conditions [27,28].

### 1.1. Experimental procedure

For validation, experimental data is used from a previous work on commercial cells [21]. Four types of commercial cells with graphite anodes are analyzed, of which two have nickel manganese cobalt oxide (NMC) cathodes, one has nickel cobalt aluminum oxide (NCA), and one has lithium iron phosphate (LFP). Table 1 provides information on the

**Table 1**  
Experimental cell information.

Battery Chemistry	Nominal Capacity (mAh)	Voltage Range (V)	Form Factor
LFP/Graphite	2600	2.0–3.6	Cylindrical 26650
NCA/Graphite	3300	2.5–4.2	Cylindrical 18650
NMC-1/Graphite	3400	2.5–4.2	Cylindrical 18650
NMC-2/Graphite	3100	2.5–4.2	Cylindrical 18650

cells investigated in this study.

The cells perform four types of duty cycles, each with a duration of 24 h, repeated daily for about 500 cycles, with intermittent capacity tests. The peak shaving (PS) duty cycle corresponds to a C/2 rate discharge and C/4 rate charge [29], where C is the ampere-hour capacity. Frequency regulation (FR) and electric vehicle (EV) duty cycles are volatile signals, with the former being energy neutral [29], while the latter biased towards discharge [30]. Baseline (BS) duty cycle is calendar aging at various states of charge (SOCs). Within each duty cycle types, various SOC ranges are investigated, comprising a total of 13 experiments for each chemistry. For each experiment, three cells are tested for a total of 156 cells.

A reference performance capacity test is performed every 30 cycles to determine degradation in capacity and energy. The capacity test is a constant current (C/2), constant voltage charge to 100% SOC, followed by a constant current discharge (C/2) to a cutoff voltage corresponding to 0% SOC. This work primarily focuses on capacity degradation, with energy degradation analysis reserved for future work.

The model's capacity degradation is compared with data. Due to computational limitations, the physics-based model focuses on the peak shaving results and is evaluated on its ability to fit the measured capacity. Meanwhile, the statistics-based model uses all duty cycles and is evaluated on its ability to predict reference performance discharge capacity for out of sample cycles.

## 2. Bottom-up model description

A pseudo 2-d model is developed using COMSOL Multiphysics® 5.4, a finite element analysis software. The first dimension is thickness along the anode, separator, and cathode, and the second pseudo dimension is along the electrode particle radius. The mesh size is automatically selected by COMSOL based on the physics, using a finer mesh closer to the separator. The heat generated is fed into the thermal module to estimate temperature rise. As a one-sided electrode is modeled, while real cells would have multiple 2-sided electrodes within a cell, heat transfer coefficients are divided by 16, assuming 8 windings in the cell.

The basic equations for the pseudo 2-d model have been described elsewhere [1,2,15,31], with the equation derivations provided in Refs. [32,33]. In addition, cathodic dissolution, SEI formation, SEI cracking related to stress, effect of cathodic dissolution on SEI formation rate, and stress-related loss of negative active material are considered.

In the pseudo-2d model, variables such as electrolyte concentration, voltage, current density, and temperature are assumed to vary only in one dimension, along the cell thickness. All active material particles are assumed to be identical spheres of diameter 18  $\mu\text{m}$  for graphite and 12  $\mu\text{m}$  for cathode. Electrode thicknesses  $L_P$  and  $L_N$  were calculated based on Ah-capacity per unit area from the literature [34].

Fig. 1 shows the model geometry.

The following coupled relationships form the basis for this work:

- Conservation of charge in the solid phase
- Conservation of species in the solid phase

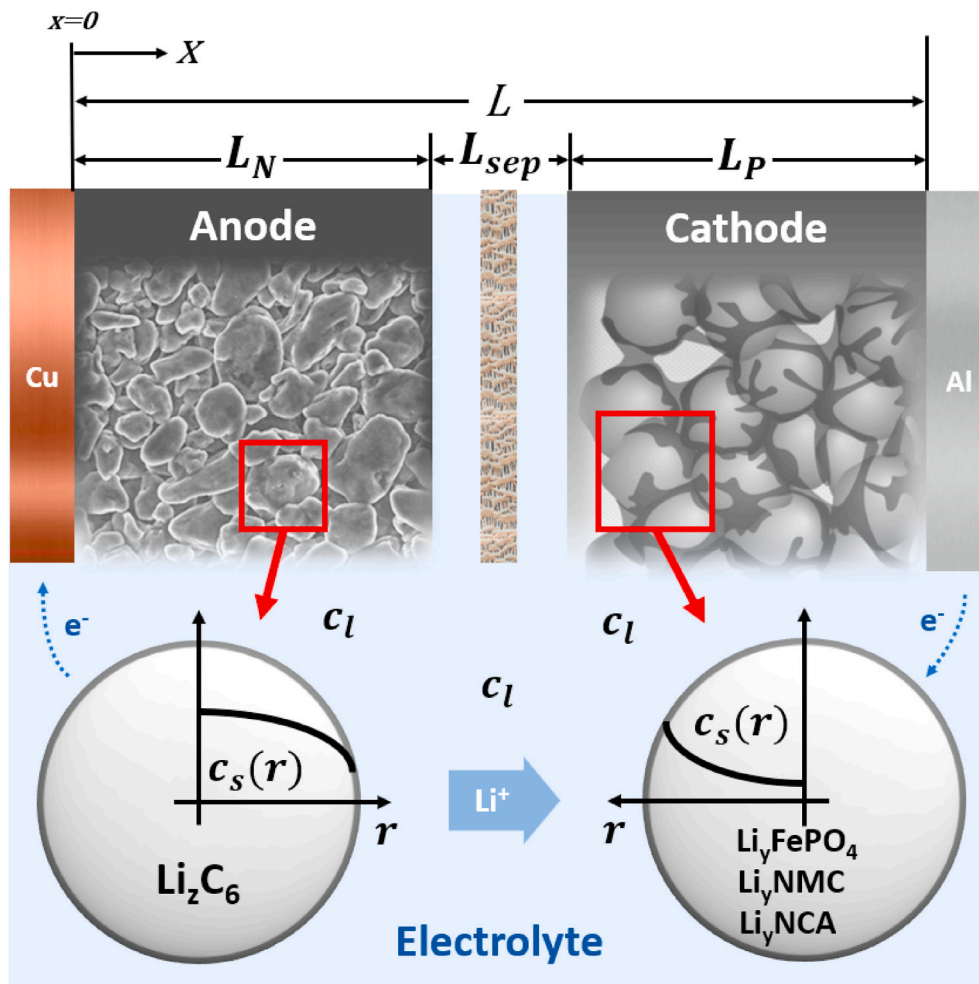


Fig. 1. Model geometry with electron and ion flow shown for charge.

- Conservation of charge in the electrolyte phase
- Conservation of species in the electrolyte
- Charge transfer at the electrode/electrolyte interface
- Heat balance

Volume fractions are defined throughout the battery by the relationship:

$$\varepsilon_l = 1 - \varepsilon_s - \varepsilon_{filler} \quad (1)$$

where  $\varepsilon_l$  is the electrolyte volume fraction (or the porosity),  $\varepsilon_s$  is the active material volume fraction in the anode or cathode, and  $\varepsilon_{filler}$  is the binder and filler volume fraction in the anode or cathode.

### 2.1. Solid phase

These equations apply to the solid phase of the anode and cathode. Conservation of charge in the solid phase:

$$\frac{\partial}{\partial x} \left( \sigma^{eff} \frac{\partial \phi_s}{\partial x} \right) - j_v = 0 \quad (2)$$

where  $\sigma^{eff}$  is the effective conductivity, which is assumed to be the electrode active material conductivity,  $\phi_s$  is the potential,  $j_v$  is the volumetric current density, and  $x$  is the coordinate along the battery thickness.

These boundary conditions correspond to the total current flowing through the current collectors:

$$-\sigma^{eff} \frac{\partial \phi_s}{\partial x} \Big|_{x=0} = \sigma^{eff} \frac{\partial \phi_s}{\partial x} \Big|_{x=L} = \frac{I}{A} \quad (3)$$

where  $L$  is the total battery thickness,  $I$  is the applied current, and  $A$  is the battery cross sectional area.

The following boundary conditions correspond to no current flow through the solid at the separator interface:

$$\frac{\partial \phi_s}{\partial x} \Big|_{x=L_N} = \frac{\partial \phi_s}{\partial x} \Big|_{x=L_N + L_{Sep}} = 0 \quad (4)$$

where  $L_N$  and  $L_{Sep}$  are the thicknesses of the negative electrode and the separator, respectively.

Conservation of species in the solid phase:

$$\frac{\partial (c_s)}{\partial t} = \frac{D_s}{r^2} \frac{\partial}{\partial r} \left( r^2 \frac{\partial c_s}{\partial r} \right) \quad (5)$$

where  $r$  is the coordinate along the particle radius and  $c_s$  is the concentration of lithium in the particle.

With boundary conditions:

$$\frac{\partial c_s}{\partial r} \Big|_{r=0} = 0 \quad (6)$$

$$\frac{\partial c_s}{\partial r} \Big|_{r=r_p} = -\frac{j_v}{a_v F} \quad (7)$$

where  $r_p$  is the particle radius,  $F$  is Faraday's constant, and  $a_v$  is the particle specific surface area (surface area per electrode volume), which is calculated from the solid volume fraction  $\varepsilon_s$  and the particle radius  $r_p$ :

$$a_v = \frac{3\varepsilon_s}{r_p} \quad (8)$$

### 2.2. Liquid phase

These equations apply to the liquid phase in the electrolyte in the anode, cathode, and separator.

Conservation of charge in the electrolyte phase leads to the following equations:

$$\frac{\partial}{\partial x} \left( k^{eff} \frac{\partial \phi_l}{\partial x} \right) - \frac{\partial}{\partial x} \left( \frac{k^{eff} 2RT}{F} \right) \left( 1 + \frac{\partial \ln f_{\pm}}{\partial \ln c_l} \right) (1 - t_+) \frac{\partial}{\partial x} \ln c_l + j_v \quad (9)$$

where  $k^{eff}$  is the effective conductivity,  $\phi_l$  is the potential,  $R$  is the ideal gas constant, and  $f_{\pm}$  is the mean molar activity coefficient.

With the boundary conditions corresponding to no current flow through the electrolyte at  $x = 0$  and  $x = L$

$$\frac{\partial \phi_l}{\partial x} \Big|_{x=0} = \frac{\partial \phi_l}{\partial x} \Big|_{x=L} = 0 \quad (10)$$

For conservation of lithium species in the electrolyte, concentrated solution theory is used to account for species transport and participation in reactions. From the positive and negative ion fluxes [1,35,36], the material balance in the electrolyte for the salt is given by:

$$\frac{\partial (\varepsilon_l c_l)}{\partial t} = -\frac{\partial \left( D_l^{eff} \frac{dc_l}{dx} \right)}{\partial x} + \frac{(1 - t_+) j_v}{F} \quad (11)$$

where  $\varepsilon_l$  is the electrolyte volume fraction,  $c_l$  is the concentration of lithium salt in the electrolyte,  $D_l^{eff}$  is the effective diffusion coefficient in the electrolyte, and  $t_+$  is the transport number.

With boundary conditions:

$$\frac{\partial c_l}{\partial x} \Big|_{x=0} = \frac{\partial c_l}{\partial x} \Big|_{x=L} = 0 \quad (12)$$

Electrode architecture governs electrode and cell behavior in several ways. The electrode porosity and tortuosity govern the rate of ion transport through the electrode depth. Tortuosity as a function of electrode porosity is different for different particle shapes [37]. The effective electrolyte conductivity and diffusivity are given by:

$$\kappa_{eff} = \kappa \frac{\varepsilon_l}{\tau} \quad (13)$$

$$D_{eff} = D \frac{\varepsilon_l}{\tau} \quad (14)$$

where  $\kappa$  is electrolyte conductivity and  $D$  is diffusion coefficient for lithium ions in electrolyte.

Tortuosity is defined for the separator and graphite [37]:

$$\tau = k \varepsilon_l^{-\alpha} \quad (15)$$

The MacMullin number  $N_m$ , the ratio of tortuosity to porosity, is provided as a function of porosity for cathode materials [37]. The tortuosity functions for separator and graphite and MacMullin number for cathode materials provided in their work are used in this model.

### 2.3. Charge transfer at the electrode/electrolyte interface

The volumetric current density at the electrode/electrolyte interface is given by the Butler Volmer equation, applicable to both electrodes:

$$j_v = a_v i_{ex} \exp \left( \frac{\alpha_a F \eta}{RT} \right) - \exp \left( \frac{-\alpha_c F \eta}{RT} \right) \quad (16)$$

where  $i_{ex}$  is the exchange current density,  $\eta$  is the overpotential and  $\alpha_a$  and  $\alpha_c$  are charge transfer coefficients for oxidation and reduction respectively, assumed to be equal to 0.5.

The exchange current density is calculated from the rate constant  $k$ :

$$i_{ex} = k \text{Mult}_{intercal} (c_{s,max} - c_{s,R})^{\alpha_a} (c_{s,R})^{\alpha_c} \left( \frac{c_l}{c_{ref}} \right)^{\alpha_a} \quad (17)$$

where  $c_{ref}$  is 1 mol m<sup>-3</sup> and  $\text{Mult}_{intercal}$  is an interaction term explained in Section 2.4.

For the graphite electrode, the cathodic overpotential during charge is reduced by the potential drop across the SEI layer:

$$\eta = \varphi_s - \varphi_l - E_{eq} - \frac{j_v}{a_v} \left( \frac{\delta_{SEI}}{k_{SEI}} \right) \quad (18)$$

where  $\varphi_s$  is solid phase potential,  $\varphi_l$  is liquid phase potential,  $E_{eq}$  is equilibrium potential,  $\delta_{SEI}$  is SEI layer thickness and  $k_{SEI}$  is SEI layer conductivity. We assume no SEI formation and hence no such correction at the cathode.

Cathode dissolution is assumed to occur at high charge potentials for layered oxide cathodes containing transition metals. Assuming the reverse reaction is negligible, the dissolution volumetric current density  $j_{v,dis}$  is given by:

$$j_{v,dis} = a_v i_{ex,dis} \exp\left(\frac{F\eta_{dis}}{RT}\right) \quad (19)$$

where  $\eta_{dis} = \varphi_s - \varphi_l - E_{eq,dis}$  and  $E_{eq,dis}$  is cathode dissolution equilibrium potential, with the solid active material volume fraction adjusted to account for the active material loss.

The SEI volumetric current density  $j_{v,sei}$ , assuming no diffusion limitation, is given by:

$$j_{v,sei} = a_v i_{ex,sei} Mult_{SEI} \exp\left(\frac{\alpha_{a,SEI} F \eta_{SEI}}{RT}\right) - \exp\left(\frac{-\alpha_{c,SEI} F \eta_{SEI}}{RT}\right) \quad (20)$$

where  $\alpha_{a,SEI}$  and  $\alpha_{c,SEI}$  are charge transfer coefficients for oxidation and reduction respectively, assumed to be equal to 0.05 and 0.95 respectively [6].  $Mult_{SEI}$  is an interaction term explained in Section 2.4. The overpotential for the SEI reaction is given by Eq. (21), with potential drop across the SEI layer reducing the overpotential available for the SEI formation reaction:

$$\eta_{SEI} = \varphi_s - \varphi_l - E_{eq,SEI} - \frac{j_v}{a_v} \frac{\delta_{SEI}}{k_{SEI}} \quad (21)$$

Assuming mixed kinetics related to charge transfer-diffusion coupling, the SEI volumetric current density is given by:

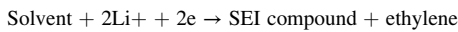
$$J_{v,SEI} = \frac{j_{v,SEI}}{1 + \frac{j_{v,SEI}}{j_{lim}}} \quad (22)$$

where  $j_{lim}$ , the limiting current density is given by:

$$j_{lim} = \frac{a_v \epsilon_s c_{solv} F D_{solv}}{\delta_{SEI}} \quad (23)$$

where  $D_{solv}$  is the diffusion coefficient of solvent in the SEI layer and  $c_{solv}$  is the solvent concentration.

The SEI compound is assumed to be lithium carbonate, forming the solid electrolyte interface by the following reaction, with the reverse reaction rate assumed to be negligible [38]:



giving the SEI layer thickness as:

$$\delta_{SEI} = \frac{M_{SEI}}{a_v F \rho_{SEI}} \int J_{v,SEI} dt \quad (24)$$

where  $M_{SEI}$  is the molar mass and  $\rho_{SEI}$  is the lithium carbonate density.

The cell performance depends on electrode porosity. The negative electrode porosity is reduced by the SEI volume as follows:

$$\Delta \epsilon_l(t) = -a_v \delta_{SEI}(t) \quad (25)$$

The change of salt concentration due to solvent consumption is accounted for, which impacts electrolyte effective conductivity and diffusivity.

## 2.4. Interactions

An interaction between the dissolved Ni from the cathode and SEI

formation is added to capture the effect of different cathodes on capacity degradation. It is assumed the dissolved Ni will migrate to the anode, increasing the SEI reaction by the following equation:

$$Mult_{SEI} = 1 + k_{nickel,SEI} n_{nickel} \quad (26)$$

where  $Mult_{SEI}$  is the multiplier applied to the SEI current  $i_{ex,SEI}$ ,  $k_{nickel,SEI}$  is a positive fitting coefficient used to relate the multiplier to  $n_{nickel}$ , the number of moles of dissolved Ni.

An interaction between the dissolved Ni and lithium intercalation into graphite is added, assuming the dissolved Ni enters the graphite, impeding intercalation:

$$Mult_{intercal} = 1 - k_{nickel,intercal} n_{nickel} \quad (27)$$

where  $Mult_{intercal}$  is the multiplier applied to  $k_{neg,Gr}$  in Eq. (17), and  $k_{nickel,intercal}$  is a positive fitting coefficient.

## 2.5. SEI formation on fresh graphite surface related to SEI cracking

Some groups have attempted to quantify graphite particle cracking, which results in fresh graphite exposure for further SEI formation [39, 40]. The limitations of such models are:

- Particles are assumed to have some fixed number of cracks, with length of cracks unchanged over time.
- These models are only valid for crack depth  $\ll$  particle radius.
- These models account for loss of lithium via SEI formation, but do not account for active material loss.

Due to these limitations, this work does not use the crack growth model. Some researchers [19,41] have used an SEI fracture model to quantify SEI formation on fresh graphite surface. Since the SEI yield strength is only a fraction of active material yield strength, this leads to frequent SEI layer breakdown, resulting in degradation rates that increase linearly with number of cycles. Since the degradation rates of cells examined decrease with increasing duration and number of cycles, this approach overestimates SEI formation rates.

We use the Kindermann et al. [6] approach to SEI cracking with the following equation:

$$j_{v,SEIcrack} = a_v i_{ex,SEI} Mult_{SEI} f_{expansion} \frac{|j_v|}{Q_v} k_{cracking} \exp\left(\frac{-\alpha_{SEI} F \eta_{SEI}}{RT}\right) \quad (28)$$

where  $f_{expansion}$  is the derivative of graphite volume as a function of lithium content using data from Hahn et al. [3],  $j_v$  is the local intercalation volumetric current density, and  $Q_v$  is the volumetric anode battery capacity in  $\text{Ah m}^{-3}$ ,  $k_{cracking}$  is a fitting constant, and  $\eta_{SEI}$  is the overpotential for the SEI formation. SEI formed via this reaction through the cracks is added to the SEI thickness as per Eq. (24).

## 2.6. Stress-related graphite active material loss

To estimate the stresses generated within graphite particles during cycling, the volume change during intercalation reported by Hahn [3] for graphite materials TIMREX® SFG6 from TIMCAL Ltd. is used. The yield stress and elastic modulus for graphite is available from Seldin [42]. Due to insufficient information on cathode active material loss related to stress cracking and to restrict the number of parameters being examined, this degradation mode was not considered for the cathode. Future work will incorporate the parameters already examined, thus giving us leeway to add parameters for stress-related cathode active material loss.

For spherical particles, the radial  $\sigma_r$  and tangential stresses  $\sigma_\theta$  are given by [9]:

$$\sigma_r(r) = \frac{2E\Omega}{9(1-\nu)} \{C_{avg}(R) - C_{avg}(r)\} \quad (29)$$

$$\sigma_{\theta}(r) = \frac{E\Omega}{9(1-\nu)} \{2C_{avg}(R) + C_{avg}(r) - 3C(r)\} \quad (30)$$

where  $E$  is the Young's Modulus,  $\Omega$  is the partial molar volume for lithium in graphite at various lithium content,  $\nu$  is Poisson's ratio, and  $C_{avg}(r)$  is the average lithium concentration within particle volume of radius  $r$  and  $C(r)$  is concentration at radius  $r$ .

The yield criterion for spherical particles is given by [9]:

$$\sigma_{ABS} = |\sigma_r - \sigma_{\theta}| \leq Y \quad (31)$$

where  $Y$  is the material yield strength and  $\sigma_{ABS}$  is the absolute value of the difference between radial and tangential stress. Since  $\sigma_{ABS}$  is maximum at the particle surface, the stress at the particle surface is used to compute  $\sigma_{ABS}$ .

The impact of repeated stresses on the particle is determined by using the fatigue criterion for the active material. The ratio of  $\sigma_{ABS}$  to yield stress is used as a proxy for fatigue [10], with a probability of failure as a function of this ratio obtained from the literature for H-451 graphite [24]. Materials that behave like metals yield when their material strength is exceeded. Once they yield, they stay in that state when the stress is removed. The active material is assumed to be ductile, and hence is expected to fail due to accumulation of fatigue during cycling. The active material particles are expected to retain some functionality even after yielding.

It is overly simplistic to assume that once a material has reached stress levels where probability of failure is 20%, that 20% of material is immediately lost. Typically, these stress levels need to be imposed for a certain amount of time. We assume a 4-h exposure is required for 20% of the material to fail at the stress corresponding to 20% probability of failure. As an example, if the particle has been exposed to 20% probability of failure for 1 h, then 5% of the particle is assumed to have failed. This 5% is removed from the particle, resulting in a higher effective current density on the remaining active material. This allows computation of failure rate at each value of  $\sigma_{ABS}$ .

## 2.7. Estimation of temperature rise in cell

The heat generated within the cell consists of reversible and irreversible heat [43], with the generation term given by Ref. [44], the first term on the right hand side being irreversible heat, and the second term reversible heat:

$$\frac{\partial Q}{\partial t} = I(V - E_{eq}) + IT \frac{\partial E_{eq}}{\partial T} \quad (32)$$

where  $E_{eq}$  is equilibrium potential.

When  $\delta E_{eq}/\delta T$  is positive, discharge is endothermic and charge is exothermic, and vice versa. The  $\delta E_{eq}/\delta T$  values for each electrode were obtained from the literature [43,45].

The heat generated is sent as input to the thermal model. A constant specific heat is used across the cell to estimate temperature rise. Heat loss to the environment via convection is incorporated on each boundary of the cell, with the loss proportional to the difference between the temperature at the boundary and the ambient.

## 2.8. 0d model

Evaluating the pseudo 2d COMSOL model is computationally intensive, taking an hour to run peak shaving tests for all four chemistries at two depths of discharge. To speed up hypothesis validation and parameter optimization, a 0D version of the model is developed making several simplifying assumptions. The 0D model calculates how much lithium is lost during aging due to SEI layer formation. This lithium loss is used to calculate the capacity loss rather than simulating a capacity reference performance test. As the capacity test is not simulated, ohmic drop across the separator and the SEI layer is ignored for calculating the

capacity, as only the amount of lithium lost is relevant. However, this ohmic drop is used for calculating the overpotentials for both the intercalation/de-intercalation and SEI formation reactions. Current is assumed to be uniformly distributed over the electrodes. The electrode overpotential is found in each electrode assuming the total current is consumed by the intercalation reactions, solving for  $\eta$  in Eq. (18). This overpotential is used to calculate the SEI reaction overpotential, which is used to calculate the SEI formation rate in the anode using Eq. (20) and Eq. (28). The cathode dissolution rate is similarly calculated in the cathode, assuming a uniform intercalation current. We calculate the overpotential from Eq. (18), from which the dissolution reaction overpotential is calculated. This dissolution overpotential is used to find the cathode dissolution rate from Eq. (19). This approximation is valid if the SEI formation current and the cathode dissolution current are negligible compared to the intercalation currents. The amount of dissolved Ni is used to increase SEI formation rate (Eq. (26)) and decrease intercalation kinetics (Eq. (27)). A limiting current density is applied based on SEI thickness and solvent diffusion rate as explained earlier in Eq. (23). Note that the graphite active material loss related to stress is ignored in the 0d model, since it is found to be negligible for the COMSOL runs. This model does not calculate the temperature or heat generated. As the model ignores current distribution in the electrolyte, it also does not capture phenomena such as electrolyte diffusion limitation brought on by pore clogging.

Evaluating this model took less than a second, allowing optimization to take place thousands of times faster than the COMSOL model.

## 2.9. Model inputs

A summary of degradation equations are provided in Table 2. The model inputs are given in Table 3 through Table 8. Most of these were used as is, while the optimized parameters shown in Table 9 used these values as the initial guess.

## 3. Results and discussion

The model is used to replicate capacity loss data for cells performing peak shaving at 20% and 60% depth of discharge (DOD), with constant power corresponding to C/4 rate charge and C/2 rate discharge at 20% SOC. The upper end of SOC was limited to 80% to prevent voltage spikes during FR and EV duty cycles that exceed cell upper voltage limit. For consistency, the same 80% upper SOC limit is maintained for peak shaving duty cycles. The cells were subjected to approximately 800 cycles over two years. Cells from four manufacturers were tested, two NMC (NMC1 and NMC2), one NCA and one LFP. The cathode composition, as measured by ICP, corresponds to a Ni content of 0.73 for NMC1, 0.85 for NCA, (with 0.05 Al) and 0.85 for NMC2. The number of moles of dissolved Ni,  $n_{nickel}$ , are calculated by multiplying the amount of cathode dissolved by the Ni content. The Al in NCA is assumed to have a stabilizing effect, with an effective Ni content assumed to be same as NMC1 at 0.73, since both cathode cells behave similarly.

Electrochemical parameters are optimized to fit the data using the Nelder-Mead algorithm [60], based on its ability to solve non-linear high dimensional optimization without calculation of derivatives. It generates a simplex that shrinks around the optimum or expands outward towards it.

The objective function feeds the input electrochemical parameters into COMSOL, records the resulting capacity degradation, and returns the root mean square error (RMSE) between the model and data. The optimization finds the parameter values which minimize this RMSE.

Several parameters in Table 3 through Table 8 are kept fixed. Preliminary simulations show graphite active material loss from stress is negligible for the currents used in our tests. Therefore, the graphite stress failure rate factor is not optimized. The electrolyte ionic conductivity and lithium transference number are fixed, since these are measured quantities reported in the literature. Cathode intercalation

**Table 2**  
Summary of degradation equations.

Equation	Description	Notes
$j_{v,SEI} = a_v i_{ex,SEI} \text{Mult}_{SEI} \exp\left(\frac{\alpha_{a,SEI} F \eta_{SEI}}{RT}\right) - \exp\left(\frac{-\alpha_{c,SEI} F \eta_{SEI}}{RT}\right) \quad (20)$	SEI formation	This is the charge transfer reaction. Eq. (22) incorporates diffusion limitation
$j_{v,SEIcrack} = a_v i_{ex,SEI} \text{Mult}_{SEI} f_{\text{expansion}} \frac{j_{v,SEI}}{Q_v} k_{\text{cracking}} \exp\left(\frac{-\alpha_{SEI} F \eta_{SEI}}{RT}\right) \quad (28)$	SEI formation through cracked SEI	This has no diffusion limitation
$j_{v,dis} = a_v i_{ex,dis} \exp\left(\frac{F \eta_{dis}}{RT}\right) \quad (19)$	Cathode dissolution	Impact of dissolved Ni on SEI formation

exchange current density is not optimized since it negligibly influences capacity loss.

Since loss of lithium is known to be the primary capacity loss mechanism, optimization focuses on issues related to SEI formation and break-up, along with the competing intercalation reaction at the graphite electrode. In addition to their importance in predicting capacity degradation, the wide range of values reported in the literature for these parameters indicate they are hard to measure directly. Therefore, choosing them in the optimization process to fit data is a more practical approach. Initial values for optimization are taken from [Table 3 through Table 8](#).

$E_{eq,SEI}$  is a key parameter determining the fraction of current going to SEI formation. Several researchers use a 0.4–0.8 V [15] equilibrium potential. In this work, 0.4 V is used as the initial value for optimization. For  $\text{Li}_2\text{C}_6$ , at  $z > 0.05$ , the open circuit voltage of the graphite electrode vs.  $\text{Li}/\text{Li}^+$  is  $< 0.2$  V vs lithium. Hence during charge, the SEI overpotential is greater than the overpotential for lithium intercalation for most of the charge duration. The SEI ionic conductivity determines the potential drop across it that reduces the overpotential available for both SEI formation and charge transfer reaction. Since  $E_{eq,SEI}$  is much more positive than the graphite equilibrium voltage at  $z > 0.05$ , this potential drop across the SEI has a greater adverse impact on intercalation overpotential and current, and results in favoring SEI formation. Other factors that affect SEI formation rate relative to lithium intercalation are also optimized. The initial SEI layer thickness is kept constant for all layered cathodes since they had a similar initial capacity loss rate. The cathode dissolution exchange current density is varied across the layered chemistries, as this is the key differentiator among layered cathodes, while fixing  $k_{\text{nickel}}$  for all chemistries. The parameters optimized are:

- $k_{\text{neg,Gr}}$ , the intercalation kinetics in graphite
- $\kappa_{SEI}$ , SEI layer ionic conductivity
- $i_{ex,SEI}$ , the SEI exchange current density
- $E_{eq,SEI}$ , the SEI formation equilibrium potential
- $k_{\text{cracking}}$ , the SEI cracking rate constant
- $\delta_{0,SEI}$ , the initial SEI thickness
- $D_{\text{solv}}$ , the solvent diffusion coefficient,
- $i_{ex,dis}$ , the cathode dissolution exchange current density
- $E_{eq,dis}$ , cathode dissolution equilibrium potential
- $k_{\text{nickel,SEI}}$ , the effect of Ni dissolved on SEI formation rate and
- $k_{\text{nickel,intercal}}$ , effect of Ni dissolved on graphite intercalation kinetics.

These parameters are optimized for the best fit across all chemistries simultaneously ([Fig. 2](#)), with all parameters related to graphite electrode and SEI kept the same across all chemistries. This results in an RMSE of 2.2%. In the final optimization,  $k_{\text{nickel,intercal}}$  and  $E_{eq,dis}$  are not optimized due to computational time requirements. [Table 9](#) shows the optimized parameter values.

Clearly, the global model does not capture the underlying degradation mechanisms adequately and has limitations in terms of fitting the degradation data for each chemistry. The degradation rates for LFP, NMC1 and NCA are slightly overestimated, while that for NMC2 is underestimated. However, the general trends are intact, with the dissolution exchange current density for the NMC2 cell 3.2 times

higher than that for the other layered chemistry cells in line with its higher capacity loss. This work assumes that the SEI formation rate is impacted only by the presence of Ni. While allowing the cathode dissolution exchange current density to vary may capture the effects of additional metals' dissolution, the specific metals, electrode architecture and design may affect how the dissolved metals impact the solvent diffusion through the SEI layer and intercalation kinetics at the graphite electrode. Hence allowing the solvent diffusion coefficient and impact of metal dissolution on intercalation kinetics to vary across chemistries may improve the quality of fit. Closer agreement with data may also be obtained with knowledge of actual electrode loading, particle size and electrode composition, a focus of our future work.

The optimized SEI layer ionic conductivity is five orders of magnitude higher than reported in the literature. The SEI formation rate is limited by solvent diffusion rate through the SEI, hence the SEI ionic conductivity is not a significant factor in determining SEI formation rate.

Optimization is also performed on each chemistry individually, with different parameters for each chemistry ([Fig. 3](#)). As expected, the fit is considerably better, with an RMSE of 1.2%. [Table 10](#) shows the optimized parameters for each chemistry.

As seen in [Tables 9 and 10](#), there are major discrepancies in the parameters chosen for the individual chemistry runs compared to the parameters needed to make the best global model. It is also highly unlikely that parameters such as intercalation rate, SEI cracking rate and SEI formation exchange current density would be different for each chemistry. Any impact on SEI exchange current density due to different metals being dissolved is expected to be captured in cathode dissolution exchange current density. However, depending on the metals dissolved, the intercalation reaction rate and diffusion coefficient for lithium through the SEI layer may be affected. Some discrepancies may be due to different electrode thicknesses and particle size. As electrode thickness and particle size are fundamental to proper modeling of cell degradation, future work will measure these parameters.

The exchange current density for cathode dissolution is the main parameter that differentiates performance among layered cathode chemistries. While the global fit does offer some indication that this value is higher for NMC2, measurement of this parameter for different metals dissolved would be useful. Experiments on measurement of lithium diffusion coefficient through SEI layers with various dissolved metals are also expected to provide useful insights.

SEI layer conductivity can be estimated from the change in internal resistance. Pulse resistance measurements were done for all cells at various states of charge during reference performance tests. Incorporating these results to extract the SEI conductivity can be done by looking at the change in resistance over time. The present model does not incorporate pulse resistance measurement results. Future work will incorporate these results and use the error in predicting the voltage curve as the objective function to optimize, enabling a better estimation of SEI layer conductivity.

There is reasonable agreement between global and individual chemistry fits for cathode dissolution,  $E_{eq,SEI}$ ,  $i_{ex,SEI}$  and  $k_{\text{neg,Gr}}$ , allowing us to assign a high level of certainty to these values. Estimation of SEI layer conductivity from pulse resistance measurements is expected to provide additional information on SEI layer ionic conductivity. This allows more leeway on optimizing solvent diffusivity and the SEI

**Table 3**  
Electrode material properties.

Parameter	Symbol	Value	Reference	Notes
Diffusion coefficient for LFP	$D_s$	Varies with lithium content	[46]	Provided as f (li) at 25 °C and 45 °C
Diffusion coefficient for NCA	$D_s$	Varies with lithium content	[47]	Used for NMC
Diffusion coefficient for LCO	$D_s$	$1 \times 10^{-10} \text{ cm}^2 \text{ s}^{-1}$	[45]	
Activation energy for NCA $D_s$	$E_a$	40 kJ mol <sup>-1</sup>	[48]	Used for LFP, NMC
Diffusion coefficient for graphite	$D_s$	Varies with lithium content	[49,50]	
Activation energy for graphite $D_s$	$E_a$	69.027 kJ mol <sup>-1</sup>	[51]	
Particle radius	$r_p$	6 μm	[6,48,51–54]	Average of references
Electrode porosity	$\epsilon_L$	0.35	[55]	
Graphite anode thickness, LFP	$L_N$	55 μm	[34]	Calculated from Ah/cm <sup>2</sup> data
Graphite anode thickness, layered cathodes	$L_N$	62 μm	[34]	Calculated from Ah/cm <sup>2</sup> data
Cathode thickness, LFP	$L_p$	57 μm	[34]	Calculated from Ah/cm <sup>2</sup> data
Cathode thickness, layered cathodes	$L_p$	76 μm	[34]	Calculated from Ah/cm <sup>2</sup> data
Tortuosity for separator, graphite	$T$	Given as function of porosity	[37]	
MacMullin Number tortuosity/porosity	$N_m$	Given as function of porosity	[37]	
Positive electrode conductivity	$\kappa_{\text{pos}}$	6.5 S m <sup>-1</sup>	[51,52,56]	Average of values in references
Negative conductivity	$\kappa_{\text{neg}}$	100 S m <sup>-1</sup>	[52]	
Maximum lithium concentration in graphite	$c_{s,\text{max,gr}}$	30.555 M	[16,17,38,57]	
Maximum lithium concentration in LFP	$c_{s,\text{max,LFP}}$	22.81 M	[17,46]	
Maximum lithium concentration in NCA	$c_{s,\text{max,NCA}}$	49.195 M	[47]	
Maximum lithium concentration in NMC	$c_{s,\text{max,NMC}}$	50.29 M	[6,16]	
Graphite density	$\rho_{\text{gr}}$	1.9 g cm <sup>-3</sup>	[52]	
Lithium manganese spinel (LMO) density <sup>a</sup>	$\rho_{\text{LMO}}$	4.14 g cm <sup>-3</sup>	[52]	
Polymer binder density	$\rho_{\text{pol}}$	1.78 g cm <sup>-3</sup>	[52]	
Electrolyte density	$\rho_e$	1.324 g cm <sup>-3</sup>	[52]	
Conductive filler density	$\rho_{\text{fil}}$	1.9 g cm <sup>-3</sup>	Our Assumption based on carbon black density	

<sup>a</sup> Used LMO density for cathode material.**Table 4**  
Solid electrolyte interface properties.

Parameter	Symbol	Value	Reference
SEI layer ionic conductivity	$\kappa_{\text{SEI}}$	$2.3 \times 10^{-6} \text{ S m}^{-1}$	[18]
Initial SEI layer thickness	$\delta_{0,\text{SEI}}$	20 nm	[6]
Lithium carbonate density	$\rho_{\text{SEI}}$	2110 kg m <sup>-3</sup>	[6]
Diffusivity of solvent through SEI layer	$D_{\text{soliv}}$	$0.2 \times 10^{-14} \text{ cm}^2 \text{ s}^{-1}$	[17]

**Table 5**  
Electrolyte properties.

Parameter	Symbol	Value	Reference
Diffusivity of lithium in electrolyte	$D_l$	Provided as function of electrolyte concentration and temperature	[58]
Transference number for lithium	$t^+$	0.363	[52], [53, 57]
Ionic conductivity of electrolyte (1- $t^+$ )(1+dlnf±/dlnC)	$\kappa_{\text{eff}}$	Given as f(electrolyte salt concentration, temperature)	[58]
Electrolyte concentration	$c_l$	1.2 M	[58]

**Table 6**  
Kinetic parameters.

Parameter	Symbol	Value	Reference	Notes
Kinetic rate constant for NCA	$k_{\text{pos}}$	$5 \times 10^{-11} \text{ mol}^{0.5} \text{ m}^{-2.5} \text{ s}^{-1}$	[48]	
Kinetic rate constant for NMC	$k_{\text{pos}}$	Assume same as NCA		
Kinetic rate constant for LFP	$k_{\text{pos}}$	Eq (5) of [46] - quadratic polynomial of geometric current density	[46]	
Exchange current density for graphite intercalation	$k_{\text{neg,Gr}}$	6.7 A m <sup>-2</sup>	[1,17,52]	Converted to kinetic rate constant
Activation energy for all rate constants	$E_a$	30 kJ mol <sup>-1</sup>	[48]	
SEI formation exchange current density	$i_{\text{ex,SEI}}$	$14.7 \times 10^4 e^{(-86.2/RT)} \text{ A m}^{-2}$	[6]	
Equilibrium potential for SEI formation	$E_{\text{eq,SEI}}$	0.4 V	[15]	
Cathode dissolution exchange current density	$i_{\text{ex,dis}}$	$6.05 \times 10^{-6} \text{ A m}^{-2}$	[6]	
Equilibrium potential for cathode dissolution	$E_{\text{eq,dis}}$	4.0 V	[6]	

cracking rate constant for global and individual chemistry fits.

Fig. 4 shows lithium content at the end of charge and discharge in both anode and cathode for all chemistries as a function of cycle number. Maximum values correspond to the end of charge for graphite, and end of discharge for cathodes, and vice versa. The lithium content of graphite at the end of charge always decreases, while lithium content in cathode also decreases. This is expected, since charging is done to a fixed 4.2 V per cell, hence as lithium content at the end of charge in graphite decreases accompanied by a rise in negative electrode potential, the

**Table 7**  
Thermal parameters.

Parameter	Symbol	Value	Reference	Notes
Volumetric heat capacity	$C_p$	$2.58 \times 10^{-11} \text{ J K}^{-1} \text{ m}^{-3}$	[48]	
Heat capacity	$C_h$	$750 \text{ J K}^{-1} \text{ kg}^{-1}$	[45]	
Planar thermal conductivity positive electrode	$k_{x-y}$	$237 \text{ W K}^{-1} \text{ m}^{-1}$	[48]	Geometric mean used
Planar thermal conductivity negative electrode	$k_{x-y}$	$401 \text{ W K}^{-1} \text{ m}^{-1}$	[48]	
Heat transfer coefficient	$h$	$70 \text{ W m}^{-2} \text{ K}^{-1}$	[17]	Using forced air cooling
Entropy term for graphite	$dE_{eq}/dT$		[45]	
Entropy term for NCA	$dE_{eq}/dT$		[47]	
Entropy term for LFP	$dE_{eq}/dT$		[43]	
Entropy term for NMC	$dE_{eq}/dT$		[43]	

**Table 8**  
Stress related parameters.

Parameter	Symbol	Value	References
SEI cracking coefficient	$k_{cracking}$	100 h	[6]
Young's modulus for graphite	$E$	10 GPa	[10]
Graphite stress failure rate constant	$r$	$0.25 \text{ h}^{-1}$	our assumption
Graphite yield strength	$Y$	23 MPa	[10]
Graphite Poisson ratio	$\nu$	0.31	[59]

**Table 9**  
Optimized parameters for all chemistries optimized together.

Quantity	Unit	NMC1	NMC2	NCA	LFP
$i_{ex,SEI}$	$\text{A m}^{-2}$	$6.36 \times 10^{-9}$	$6.36 \times 10^{-9}$	$6.36 \times 10^{-9}$	$6.36 \times 10^{-9}$
$i_{ex,dis}$	$\text{A m}^{-2}$	$1.00 \times 10^{-8}$	$3.16 \times 10^{-8}$	$1.00 \times 10^{-8}$	Not applicable (NA)
$\kappa_{SEI}$	$\text{S m}^{-1}$	0.3	0.3	0.3	0.3
$D_{solv}$	$\text{m}^2 \text{ s}^{-1}$	$5.79 \times 10^{-21}$	$5.79 \times 10^{-21}$	$5.79 \times 10^{-21}$	$5.79 \times 10^{-21}$
$k_{cracking}$	H	214	214	214	214
$E_{Eq,SEI}$	V	0.340	0.340	0.340	0.340
$\delta_{0,SEI}$	M	$1.65 \times 10^{-8}$	$1.65 \times 10^{-8}$	$1.65 \times 10^{-8}$	$2.60 \times 10^{-10}$
$k_{neg,Gr}$	$\text{m s}^{-1}$	$3.89 \times 10^{-12}$	$3.89 \times 10^{-12}$	$3.89 \times 10^{-12}$	$3.89 \times 10^{-12}$
$k_{nickel,SEI}$	$\text{mol}^{-1} \text{ m}^{-2}$	53.9	53.9	53.9	NA

positive electrode potential is also driven higher, accompanied by a lower lithium content in the cathode at the end of charge. For LFP cathodes, the minimum lithium at the end of charge is 0 as expected. At the end of discharge, lithium content in graphite is 0, while lithium content in the cathode decreases with cycles, due to lithium loss via SEI layer formation. Charge capacity is determined by cathode potential driven higher related to loss of lithium, and discharge capacity by anode potential driven higher as lithium gets exhausted at the end of discharge. While the maximum lithium content at the end of charge in graphite and at the end of discharge in cathode is decreasing at the same rate for LFP, the maximum lithium content decreases at a lower rate for layered cathodes at the end of discharge. This is especially obvious for NMC2, for which the maximum lithium content appears to approach a minimum, as cathode active material loss due to Ni dissolution counters loss of lithium due to SEI formation at the anode.

As Ni dissolves from the positive electrode, the cathode capacity decreases proportionately. The lithium content in graphite at the end of charge decreases each cycle, increasing its potential. To maintain the same end of charge voltage, the cathode potential also increases with each cycle, resulting in lower lithium content at the end of each charge, and therefore greater dissolution rate of cathode. If cathode capacity loss is less than the loss of lithium via SEI formation, discharge termination occurs when graphite is exhausted of lithium. The cathode dissolution rate may eventually cause greater cathode capacity loss than loss of lithium due to SEI formation. In that event, during subsequent discharge, when the anode is emptied of lithium, the cathode lithium starts to increase with cycles, resulting in a decrease of cathode electrode potential. This happens until the cathode lithium content reaches its maximum value. After this, the cathode capacity determines the discharge capacity, not loss of lithium. Simulation through 2000 cycles does not show this effect. Future work will explore the effect of increasing the upper SOC limit on maximum lithium content in the cathode as a function of cycles.

Layered cathodes get less stable when lithium content decreases below a minimum threshold. This model does not attempt to capture this effect. Future work will incorporate the impact of cycling to low lithium content during the charge on the battery state of health.

The difference in degradation rate may be entirely explained by dissolved Ni if a suitable function relating SEI formation rate to dissolved Ni can be derived. In this work, this effect appears to be underestimated, as the experimentally determined capacity loss varies more between chemistry than in the COMSOL model. This may partially be due to overestimation of SEI layer resistance and underestimation of cathode dissolution exchange current density for NMC2 cells. However, when comparing the discharge energy capacity lost as a function of Ah capacity loss, the NMC cells exhibit a similar trend, implying similar increases in internal resistance (Fig. S1). By contrast, for LFP and NCA, the slope of discharge energy capacity vs. Ah capacity loss is higher, showing a larger increase in internal resistance. This indicates that the SEI resistance could be overestimated for NMC1 and NMC2 and/or underestimated for LFP and NCA, and the cathode dissolution rate for NMC2 is being underestimated.

Fig. 5 shows the SEI layer formation rate for each chemistry for the global fit. With increasing cycles, LFP SEI formation rate is constant as  $f$  (voltage), while the layered oxide SEI formation rate increases at all voltage levels, especially at high voltage levels. This is because the dissolution rate increases exponentially at high voltage levels, which is accompanied by a higher SEI formation rate. With increasing cycles, as the SEI layer thickness grows, diffusion limitation through the SEI layer reduces SEI formation rate. The results for the cathode dissolution rate are shown in Fig. S2.

Fig. 6 shows the fraction of original capacity lost from each mechanism for all layered cathode cells. Due to greater dissolution exchange current density, the Ni dissolved is highest for NMC2 cathode cells, accompanied by higher loss from SEI formation. Graphite active material loss due to cracking is negligible for all cells due to low currents.

Despite being significantly simpler, the 0D model fit the data better across all chemistries than the pseudo-2d COMSOL model, as seen in Fig. 7 with an RMSE of 1.0%. This may be because it can do more iterations in a shorter time, allowing for better optimization, which is vital when there are complicated interactions between the input parameters. As computational time was not an issue, more parameters could be optimized, such as  $E_{Eq,dis}$  and initial quantity of cathode dissolved. Due to its superior ability to fit the data, our hypothesis that the varying degradation rates of cells with layered cathodes are due to differences in cathode dissolution rates and the effect of dissolved Ni on SEI formation is supported by the 0D model, even with a simplistic linear dependence of SEI formation rate on dissolved Ni. The optimized parameters for the 0d model are shown in Table 11.

COMSOL is also prone to instability and crashing when certain parameters are set too low, unlike the 0D model. As the 0d model selects

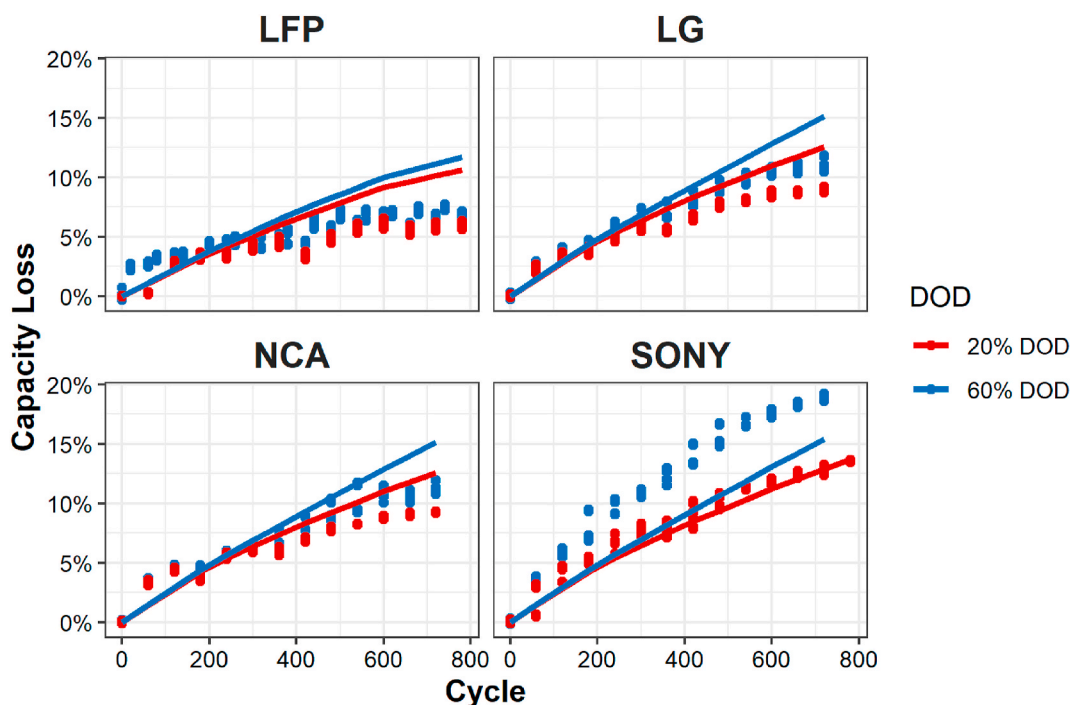


Fig. 2. Best fit for all chemistries using different cathode dissolution rate for each chemistry.

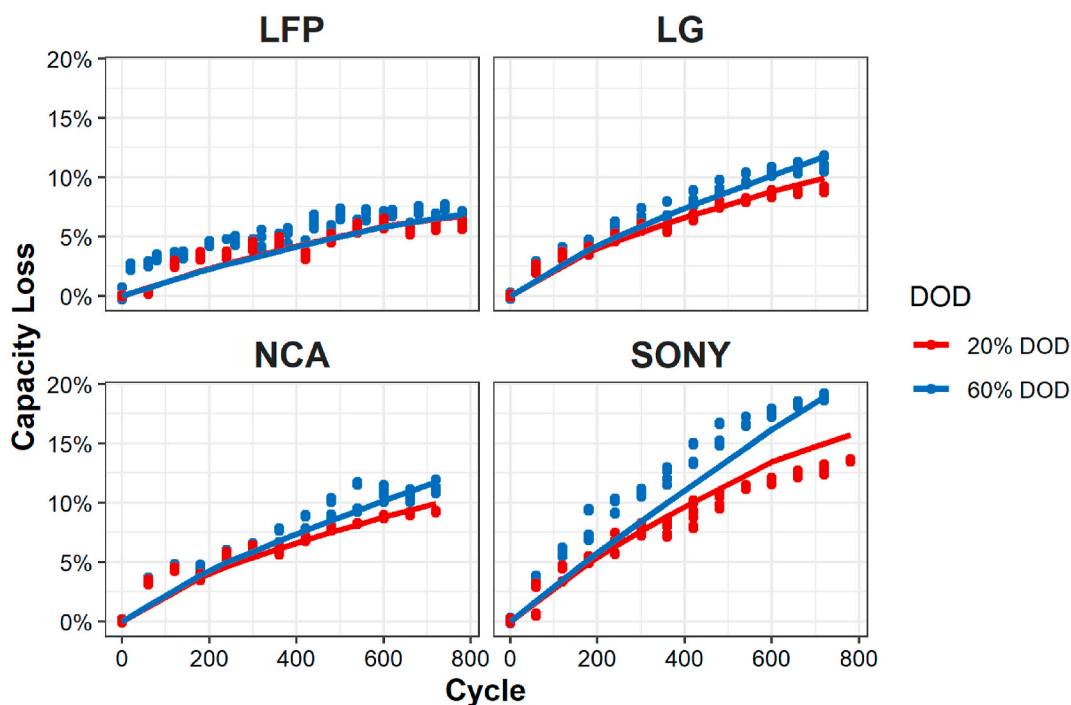


Fig. 3. Best fitting model for individual chemistries, using different parameters for each chemistry.

much lower values for SEI exchange current density, solvent diffusivity in the SEI and graphite intercalation kinetics than COMSOL could handle, COMSOL’s inability to explore these parameter values may have hurt its ability to fit the data. This is reflected in only a factor of three separating dissolution exchange current density for the COMSOL model, while this parameter spans ten orders of magnitude in the 0d model. The five orders of magnitude lower SEI exchange current density and two orders of magnitude lower  $k_{cracking}$  help reduce the overestimation of degradation in LFP cells, while the larger range of cathode dissolution

exchange current density coupled with two orders of magnitude higher  $k_{nickel,SEI}$  remove underestimation of degradation for layered cathode cells, especially NMC2. Note that the 0d model selects different equilibrium potentials than the COMSOL model. This results in the effective SEI formation current and cathode dissolution current increasing by approximately a factor of 5 and 15 respectively for the 0d model, due to the difference in equilibrium potentials, as the current for a given reaction is proportional to  $\exp\left(\frac{E_{eq}F}{RT}\right)$  (see Eq (2.19)). This shows the

**Table 10**  
Optimized parameters for individual chemistries optimized separately.

Quantity	Unit	NMC1	NMC2	NCA	LFP
$i_{ex,SEI}$	$A m^{-2}$	$6.43 \times 10^{-9}$	$1.21 \times 10^{-8}$	$6.43 \times 10^{-9}$	$4.22 \times 10^{-9}$
$i_{ex,dis}$	$A m^{-2}$	$1.01 \times 10^{-8}$	$3.06 \times 10^{-8}$	$1.01 \times 10^{-8}$	NA
$\kappa_{SEI}$	$S m^{-1}$	0.3	0.032	0.3	0.3
$D_{solv}$	$m^2 s^{-1}$	$7.73 \times 10^{-21}$	$5.86 \times 10^{-21}$	$7.73 \times 10^{-21}$	$2.71 \times 10^{-21}$
$k_{cracking}$	H	217	183	217	191
$E_{Eq,SEI}$	V	0.335	0.335	0.335	0.34
$\delta_{0,SEI}$	M	$1.60 \times 10^{-8}$	$1.62 \times 10^{-8}$	$1.60 \times 10^{-8}$	$5.52 \times 10^{-10}$
$k_{neg,Gr}$	$m s^{-1}$	$3.94 \times 10^{-12}$	$4.05 \times 10^{-12}$	$3.94 \times 10^{-12}$	$7.43 \times 10^{-12}$
$k_{nickel,SEI}$	$mol^{-1} m^{-2}$	55	66	55	NA

importance of measuring cathode dissolution equilibrium potential, as dissolution current has an exponential dependence.

Future work will develop this model to capture more phenomena from the pseudo-2d COMSOL model such as active material stress and heat generation, lithium plating, simulating a capacity test instead of just counting lithium lost. The model will also be applied to all the duty cycles tested instead of just peak shaving.

The 0d model is used to find how sensitive the capacity degradation was to each parameter in Table 11. Each parameter from Table 11 is varied from one order of magnitude smaller than its optimum value to one order of magnitude larger than its optimum value.

The total capacity degradation magnitude is most sensitive to  $k_{neg}$ ,  $i_{ex,SEI}$ ,  $D_{solv}$ , and  $i_{ex,dis}$ . We are also interested in characterizing the shape of the capacity loss over time. Therefore, we fit a power law to characterize the resulting capacity degradation behavior:

$$\ln Caploss = c_1 \ln n + c_2 DOD + c_3 \quad (33)$$

where  $n$  is the number of cycles, and  $c_i$  are fitting coefficients. We look at how these coefficients vary with varying electrochemical parameters to understand their impact. The coefficient  $c_2$  captures how the capacity

loss depends on the duty cycle's DOD. It is most sensitive to  $k_{neg}$ , followed by  $D_{solv}$ , and  $i_{ex,SEI}$ . The exponential coefficient  $c_1$  gives the power law exponent, and thus how the capacity loss levels off with time. It is impacted most by  $k_{neg}$ ,  $i_{ex,SEI}$ ,  $k_{nickel,SEI}$ , and  $i_{ex,dis}$ .

#### 4. Top down model

As discussed in the previous section, the COMSOL pseudo 2d physics-based model is unable to satisfactorily replicate the capacity degradation of all chemistries we have examined. Therefore, a statistics-based model is developed for accurately predicting capacity degradation. This also has the advantage of very fast computation, so it is straightforward to try different model recipes and statistical tests compared to a finite element analysis model.

The cells were subjected to various duty cycles, including PS, FR, EV, and BS. The rate of capacity loss depends on voltage, current, and SOC:

$$\frac{dCaploss}{dt} = f(V, I, SOC) \quad (34)$$

Integration of both sides yields Eq. (35), which allows regression of any coefficients in the function to fit the observed capacity loss.

$$Caploss = \int f(V, I, SOC) dt \quad (35)$$

Functions are evaluated by their ability to predict capacity loss in future cycles, using a model trained on data from previous cycles. As the capacity test took place every 30 cycles, the model predicts at least 30 cycles ahead. One function is tested for each chemistry. The same function and coefficients are used for all duty cycles associated with each service, ensuring the model is tested across a wide range of conditions.

For the first iteration of the model, the rate of capacity loss is assumed to be quadratic with respect to current and cubic with respect to voltage, along with their interactions. Fitting power series coefficients allows us to capture most physical phenomenon, although going beyond cubic is assumed to add too much complexity, running the risk of overfitting. Any increased complexity should be added using more physical insights about the underlying phenomena. As shown by the

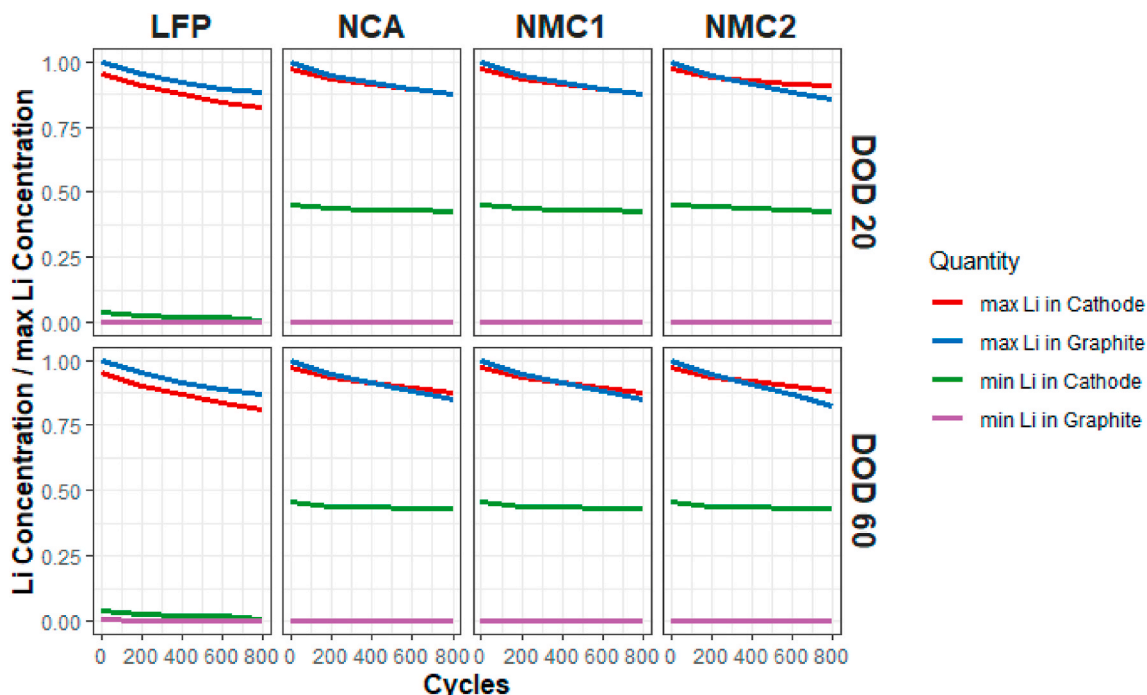


Fig. 4. Maximum and minimum lithium content as function of cycles in each electrode for global model.

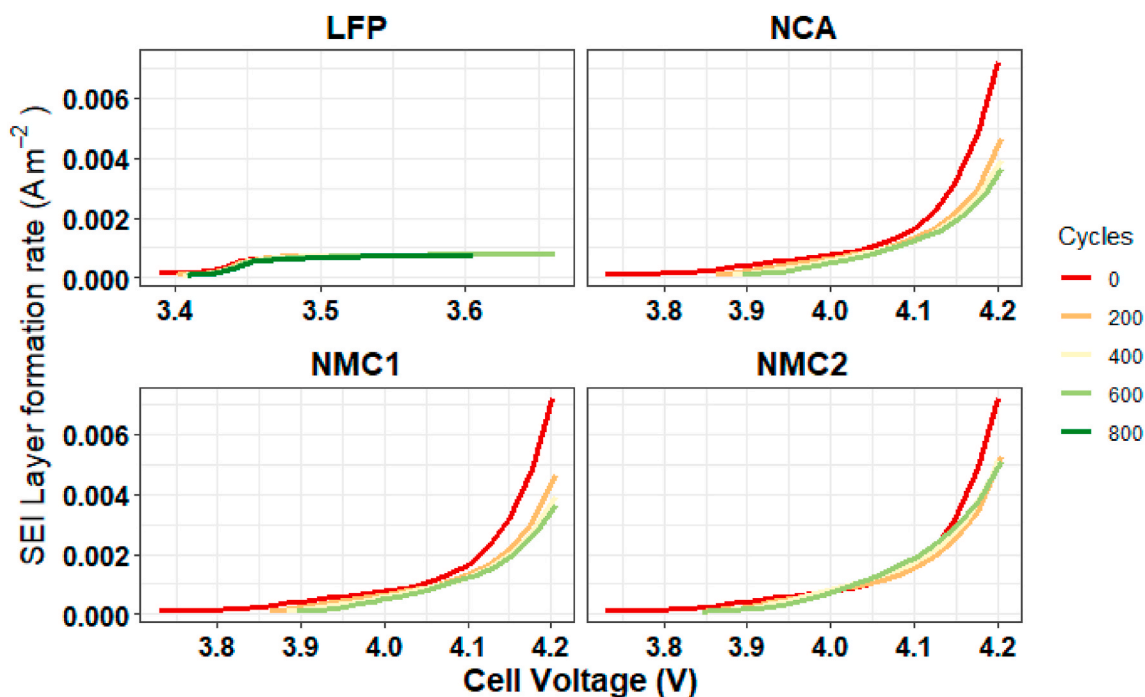


Fig. 5. SEI formation rate as function of voltage.

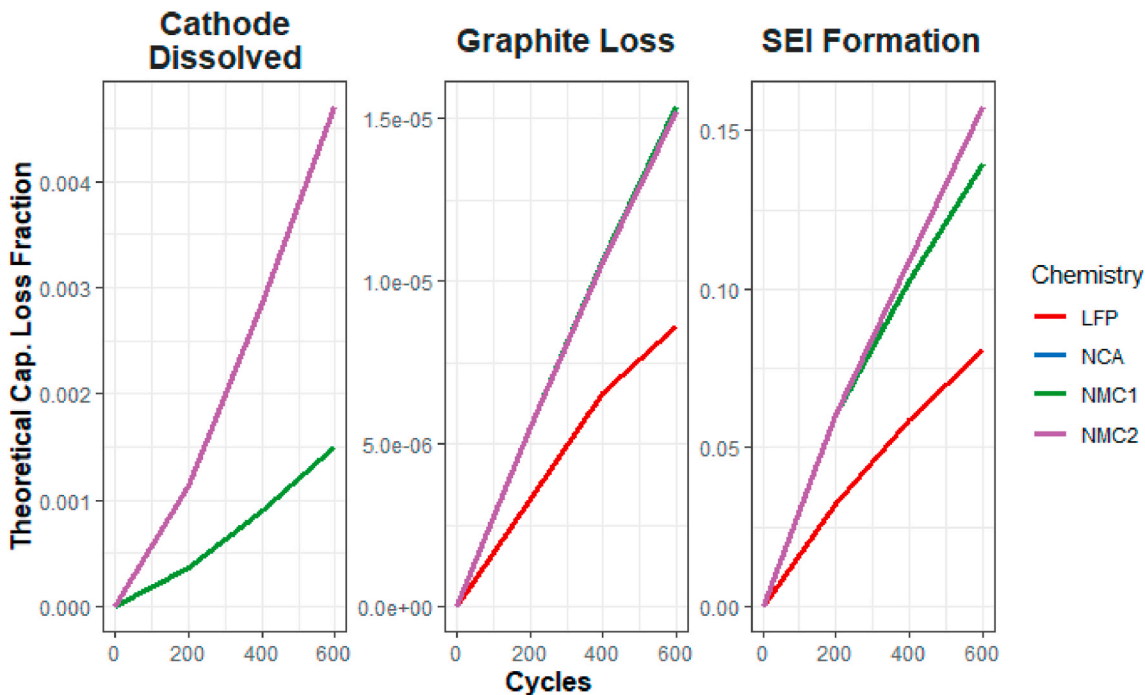


Fig. 6. Loss from each mechanism as function of cycle number for global fit.

physics-based model, the cell (and individual electrode voltage) is extremely important in determining cathode dissolution and SEI formation rate. Hence, the extra cubic term is added to voltage. Since voltage itself is a function of current, we limit the current terms.

$$\frac{dCaploss}{dt} \sim (1 + I + I^2) \times (1 + V + V^2 + V^3) \tag{36}$$

This model is checked for overfit by dropping each term individually and observing the out of sample error. Across all chemistries, every term increases out of sample error if dropped, whether predicting 30 or 150

cycles ahead. This implies some underfit.

Applying lessons from the physics to the statistics-based model, the effect of graphite stress and SEI breakdown is incorporated. We take the first and second derivatives of the volumetric expansion of graphite as a function of lithium content (or SOC), with respect to the lithium content. The first derivative captures the stress of the particle expanding or contracting, and the second derivative captures the effect of differential expansion or contraction across the graphite particle. Each of these derivatives are interacted with current, which is a proxy for the rate of expansion or contraction. The resulting equation is:

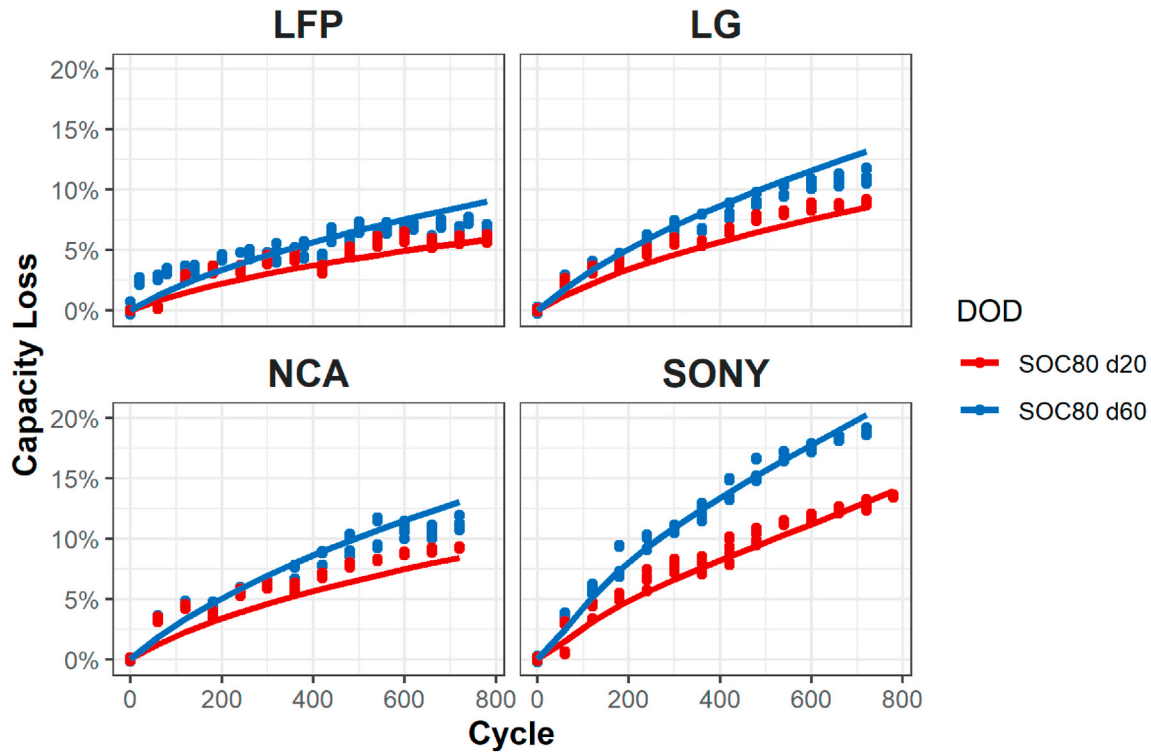


Fig. 7. 0d model applied to all chemistries.

**Table 11**  
Optimized parameters for all chemistries together in 0d model.

Quantity	Unit	NMC1	NMC2	NCA	LFP
$i_{ex,SEI}$	$A m^{-2}$	$9.68 \times 10^{-14}$	$9.68 \times 10^{-14}$	$9.68 \times 10^{-14}$	$9.68 \times 10^{-14}$
$i_{ex,dis}$	$A m^{-2}$	$2.01 \times 10^{-8}$	$1.56 \times 10^{-3}$	$5.39 \times 10^{-13}$	NA
$k_{SEI}$	$S m^{-1}$	0.30	0.30	0.30	0.30
$D_{solv}$	$m^2 s^{-1}$	$8.32 \times 10^{-23}$	$8.32 \times 10^{-23}$	$8.32 \times 10^{-23}$	$8.32 \times 10^{-23}$
$k_{cracking}$	H	0.23	0.23	0.23	0.23
$E_{Eq,SEI}$	V	0.382	0.382	0.382	0.382
$\delta_{0,SEI}$	m	$3.08 \times 10^{-14}$	$3.08 \times 10^{-14}$	$3.08 \times 10^{-14}$	0
$k_{neg,Gr}$	$m s^{-1}$	$1.19 \times 10^{-13}$	$1.19 \times 10^{-13}$	$1.19 \times 10^{-13}$	$1.19 \times 10^{-13}$
$k_{nickel,SEI}$	$mol^{-1} m^{-2}$	$3.83 \times 10^3$	$3.83 \times 10^3$	$3.83 \times 10^3$	NA
$E_{Eq,dis}$	V	4.07	4.07	4.07	NA
Initial amount of cathode dissolved	1	$1.00 \times 10^{-3}$	$1.00 \times 10^{-3}$	$1.00 \times 10^{-3}$	NA

$$\frac{dCaploss}{dt} \sim (1 + I + I^2) \times (1 + V + V^2 + V^3) + I \frac{dvol}{dc_{Li}}(SOC) + I \frac{d^2vol}{dc_{Li}^2}(SOC) \quad (37)$$

The same test is performed by looking at the out of sample error with or without each term. The stress terms not only reduce the out of sample error but removing them increases the error more than any of the other terms, implying they are strongly capturing the effect of degradation. Without the stress terms, the RMSE predicting 30 cycles ahead is 1%, while with them, it decreases to 0.8%. The results are shown in Fig. 8.

The elasticnet algorithm upgrades the model with machine learning. This algorithm produces an interpretable formula with coefficients like linear regression does, but with a penalty assigned to larger coefficients, reducing the model's tendency to read too much into any individual variable, reducing overfit. Elasticnet can use the same formula from Eq. (37), reducing error from overfitting. Elasticnet gives a consistently

lower out of sample error for all chemistries and all cycles predicted ahead, demonstrating there are some overfitting issues in the initial MLR. The error is reduced to 0.6% out of sample for 30 cycles ahead, and 0.7% for 150 cycles ahead. The prediction comparison for 150 cycles ahead is shown in Fig. 8.

The statistical model performs well across a wide range of operating conditions, without considering one important phenomenon - the capacity loss leveling off due to solvent diffusion limitation in the SEI layer. This will be left to future work.

## 5. Conclusion

We have developed both physics-based and statistics-based state of health models and validated them using single cell data. Insights from the physics-based model are used in the statistical approach and shown to increase model accuracy.

Computational time continues to be the bottle neck for physics-based modeling, hence future work may move away from using COMSOL and towards more optimized code, building on the 0d model. Our hypothesis on interaction between cathode dissolution and SEI layer formation appears to be validated for explaining why different cells with cathode chemistries degrade at different rates. More instructive is the fact that  $E_{Eq,SEI}$  and  $i_{ex,SEI}$  values are similar across all models, thus providing reliability to these estimates. The ability to explore lower values for  $i_{ex,SEI}$ ,  $D_{solv}$  and  $k_{neg,Gr}$  allows a greater range of cathode dissolution exchange current density  $i_{ex,dis}$  for layered cathodes. This shows that by overcoming computational time limitations in COMSOL, more accurate simulations are possible. Future work will also look at the other duty cycles applied to single cell data apart from peak shaving.

This bottleneck of computational time is informative for high level modeling considerations as well. While it took a lot of time to get an acceptable pseudo 2d COMSOL model that predicts the results after considering the relevant mechanisms, the work to set up a 0d model was very fast by comparison. Starting with a simple model allows fast testing with each added complexity, making the work more efficient. By contrast, attempts to simplify the COMSOL model were much less

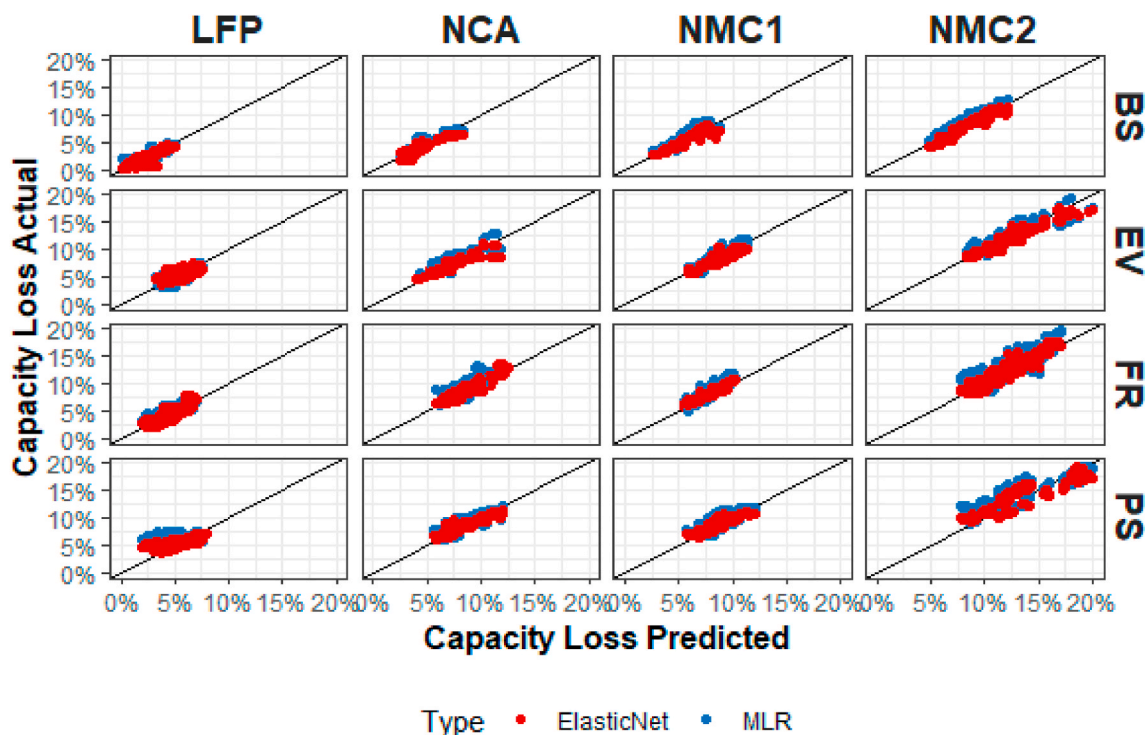


Fig. 8. Statistical model predictions 150 cycles ahead for multilinear regression (MLR, blue) and elasticnet (red). (For interpretation of the references to colour in this figure legend, the reader is referred to the Web version of this article.)

fruitful, since it was unknown which pieces of model complexity were vital and which weren't. Furthermore, the long runtime made for difficult testing. The COMSOL battery module itself is highly complex even before degradation mechanisms are added, which makes high dimensional optimization difficult. We recommend modelers also use a simple starting approach, and add complexity sequentially, ensuring each added complexity improves the model's accuracy.

The statistics-based model is fast and robust, and by using elasticnet, machine learning can be used to increase predictive capability without sacrificing interpretability. Future work will focus on incorporating more insights from the physics-based model, especially SEI layer diffusion limitation.

For both models, we have concentrated on capacity degradation, yet energy degradation is also important, especially as the internal resistance increases as the battery degrades. Future work will also predict energy degradation and incorporate internal resistance measurement results. We also plan to expand our analysis to new datasets to ensure the model can generalize.

This work also identifies parameters most sensitive for experimentalists to measure. For example, as the degradation reactions such as SEI formation and cathode dissolution vary exponentially with their equilibrium potential, it is vital to precisely experimentally measure these quantities. Furthermore, the interaction of dissolved cathode with the SEI layer formation is incredibly important. Experimental work should focus on the role of each dissolved metal on SEI formation kinetics, solvent diffusivity in SEI, and intercalation rate.

Code for both models can be found at <https://github.com/PNNL-Reliability/State-of-health> containing the entire statistics-based model, the 0d physics based model, and code to run the COMSOL model (requires a COMSOL purchase to operate).

## Appendix A. Supplementary data

Supplementary data to this article can be found online at <https://doi.org/10.1016/j.jpowsour.2021.230032>.

## CRediT authorship contribution statement

**Alasdair J. Crawford:** Methodology, Software, Validation, Formal analysis, Data curation, Writing – original draft, Visualization. **Daiwon Choi:** Methodology, Validation, Investigation, Resources. **Patrick J. Balducci:** Project administration, Funding acquisition. **Venkat R. Subramanian:** Validation, Writing – review & editing. **Vilayanur V. Viswanathan:** Conceptualization, Methodology, Writing – original draft, Writing – review & editing.

## Declaration of competing interest

The authors declare that they have no known competing financial interests or personal relationships that could have appeared to influence the work reported in this paper.

## Acknowledgements

The authors acknowledge the financial support from the U.S. Department of Energy (DOE) Office of Electricity Delivery and Energy Reliability (OE). We acknowledge the individual cell data for all duty cycles provided by the PNNL Safety & Reliability Program funded by the US DOE Office of Electricity. We are grateful for useful discussions on mechanical stress and particle failure with Dr. Vineet Joshi, Materials Scientist at Pacific Northwest National Laboratory, and Andrew Keane, Mechanical Engineer. We are also grateful for guidance provided by Dr. Imre Gyuk, the program manager of the Energy Storage and Power Electronics Program at DOE-OE. Pacific Northwest National Laboratory is a multiprogram national laboratory operated for the DOE by Battelle under Contract DE-AC05-76RL01830.

## Nomenclature

### Acronyms

BESS	battery energy storage system
BS	baseline
DOD	depth of discharge
EV	electric vehicle
FR	frequency regulation
LFP	lithium iron phosphate
NCA	nickel cobalt aluminum oxide
NMC	nickel manganese cobalt oxide
PS	peak shaving
RMSE	root mean square error
SEI	solid electrolyte interphase
SOC	state of charge

### Symbols

A	cross-sectional area ( $\text{m}^2$ )
$c_s$	concentration of lithium in the active material particle ( $\text{mol m}^{-3}$ )
$c_{\text{solv}}$	concentration of solvent ( $\text{mol m}^{-3}$ )
D	Diffusion coefficient ( $\text{m}^2 \text{s}^{-1}$ )
$f_{\pm}$	mean molar activity coefficient
F	Faraday's constant ( $\text{A s mol}^{-1}$ )
$i_{\text{ex}}$	exchange current density ( $\text{A m}^{-2}$ )
I	applied current (A)
$j_{\text{lim}}$	limiting current density ( $\text{A m}^{-2}$ )
$j_v$	volumetric current density ( $\text{A m}^{-3}$ )
$j_{\text{vdis}}$	dissolution volumetric current density ( $\text{A m}^{-3}$ )
$k_{\text{cracking}}$	SEI cracking rate constant (h)
$k_{\text{nickel,SEI}}$	effect of nickel dissolved on SEI formation rate ( $\text{m}^2 \text{mol}^{-1}$ )
$k_{\text{SEI}}$	SEI layer conductivity ( $\text{S m}^{-1}$ )
$L_N$	thicknesses of the negative electrode (m)
$L_p$	thicknesses of the positive electrode (m)
$L_{\text{Sep}}$	thickness of the negative electrode and the separator (m)
M	molecular weight ( $\text{kg mol}^{-1}$ )
$\text{Mult}_{\text{SEI}}$	multiplier applied to the SEI current associated with cathode nickel dissolution
Nm	MacMullin number
r	co-ordinate along particle radius (m)
$r_p$	particle radius (m)
x	co-ordinate along thickness (m)

### Greek

$\alpha_a$	charge transfer coefficients for oxidation
$\alpha_c$	charge transfer coefficients for reduction
$\epsilon_l$	volume fraction of the electrolyte
$\epsilon_s$	volume fraction of the active material in the anode or cathode
$\epsilon_{\text{filler}}$	volume fraction of the binder and filler in the anode or cathode
$\eta$	overpotential (V)
$\Phi$	potential (V)
$\sigma^{\text{eff}}$	effective conductivity ( $\text{S m}^{-1}$ )

### Subscript

l	liquid phase
s	solid active material
filler	binder and filler

## References

- [1] M. Doyle, T.F. Fuller, J. Newman, Modeling of galvanostatic charge and discharge of the lithium/polymer/insertion cell, *J. Electrochem. Soc.* 140 (6) (1993) 1526–1533.
- [2] T.F. Fuller, M. Doyle, J. Newman, Relaxation phenomena in lithium-ion-insertion cells, *J. Electrochem. Soc.* 141 (4) (1994) 982–990.
- [3] M. Hahn, H. Buqa, P.W. Ruch, D. Goers, M.E. Spahr, J. Ufheil, et al., A dilatometric study of lithium intercalation into powder-type graphite electrodes, *Electrochem. Solid St.* 11 (9) (2008) A151–A154.
- [4] C. Liu, Y. Gao, L. Liu, Toward safe and rapid battery charging: design optimal fast charging strategies through a physics-based model considering lithium plating, *Int. J. Energy Res.* 45 (2) (2021) 2303–2320.
- [5] H. Ekström, G. Lindbergh, A model for predicting capacity fade due to SEI formation in a commercial graphite/LiFePO<sub>4</sub> cell, *J. Electrochem. Soc.* 162 (6) (2015) A1003–A1007.
- [6] F.M. Kindermann, J. Keil, A. Frank, A. Jossen, A SEI modeling approach distinguishing between capacity and power fade, *J. Electrochem. Soc.* 164 (12) (2017) E287–E294.

- [7] H. Ge, T. Aoki, N. Ikeda, S. Suga, T. Isobe, Z. Li, et al., Investigating lithium plating in lithium-ion batteries at low temperatures using electrochemical model with NMR assisted parameterization, *J. Electrochem. Soc.* 164 (6) (2017) A1050–A1060.
- [8] X.-G. Yang, Y. Leng, G. Zhang, S. Ge, C.-Y. Wang, Modeling of lithium plating induced aging of lithium-ion batteries: transition from linear to nonlinear aging, *J. Power Sources* 360 (2017) 28–40.
- [9] Y.-T. Cheng, M.W. Verbrugge, Diffusion-Induced stress, interfacial charge transfer, and criteria for avoiding crack initiation of electrode particles, *J. Electrochem. Soc.* 157 (4) (2010) A508–A516.
- [10] A. Sarkar, P. Shrotriya, A. Chandra, Simulation-driven selection of electrode materials based on mechanical performance for lithium-ion battery, *Materials* 12 (5) (2019) 831.
- [11] P.M. Gomadam, J.W. Weidner, R.A. Dougal, R.E. White, Mathematical modeling of lithium-ion and nickel battery systems, *J. Power Sources* 110 (2) (2002) 267–284.
- [12] M.B. Pinson, M.Z. Bazant, Theory of SEI formation in rechargeable batteries: capacity fade, accelerated aging and lifetime prediction, *J. Electrochem. Soc.* 160 (2) (2013) A243–A250.
- [13] D. Li, D. Danilov, Z. Zhang, H. Chen, Y. Yang, P.H.L. Notten, Modeling the SEI formation on graphite electrodes in LiFePO<sub>4</sub> batteries, *J. Electrochem. Soc.* 162 (6) (2015) A858–A869.
- [14] L. Liu, M. Zhu, Modeling of SEI layer growth and electrochemical impedance spectroscopy response using a thermal-electrochemical model of Li-ion batteries, *ECS Transact.* 61 (27) (2014) 43–61.
- [15] P. Ramadass, B. Haran, P.M. Gomadam, R. White, B.N. Popov, Development of first principles capacity fade model for Li-ion cells, *J. Electrochem. Soc.* 151 (2) (2004) A196–A203.
- [16] A. Awarke, S. Pischinger, J. Ogrzewalla, Pseudo 3D modeling and analysis of the SEI growth distribution in large format Li-ion polymer pouch cells, *J. Electrochem. Soc.* 160 (1) (2013) A172–A181.
- [17] E. Prada, D. Di Domenico, Y. Creff, J. Bernard, V. Sauvant-Moynot, F. Huet, A simplified electrochemical and thermal aging model of LiFePO<sub>4</sub>-graphite Li-ion batteries: power and capacity fade simulations, *J. Electrochem. Soc.* 160 (4) (2013) A616–A628.
- [18] R. Fu, S.-Y. Choe, V. Agubra, J. Fergus, Development of a physics-based degradation model for lithium ion polymer batteries considering side reactions, *J. Power Sources* 278 (2015) 506–521.
- [19] I. Laresgoiti, S. Käbitz, M. Ecker, D.U. Sauer, Modeling mechanical degradation in lithium ion batteries during cycling: solid electrolyte interphase fracture, *J. Power Sources* 300 (2015) 112–122.
- [20] A. Wang, S. Kadam, H. Li, S. Shi, Y. Qi, Review on modeling of the anode solid electrolyte interphase (SEI) for lithium-ion batteries, *npj Comput. Mater.* 4 (1) (2018) 15.
- [21] A.J. Crawford, Q. Huang, M.C.W. Kintner-Meyer, J.G. Zhang, D.M. Reed, V. L. Sprinkle, et al., Lifecycle comparison of selected Li-ion battery chemistries under grid and electric vehicle duty cycle combinations, *J. Power Sources* 380 (2018) 185–193.
- [22] P. Arora, R.E. White, M. Doyle, Capacity fade mechanisms and side reactions in lithium-ion batteries, *J. Electrochem. Soc.* 145 (10) (1998) 3647–3667.
- [23] M. Wohlfahrt-Mehrens, C. Vogler, J. Garche, Aging mechanisms of lithium cathode materials, *J. Power Sources* 127 (1–2) (2004) 58–64.
- [24] X. Fang, H. Wang, S. Yu, The stress and reliability analysis of HTR's graphite component, *Sci. Technol. Nucl. Install.* (2014) 8, 2014.
- [25] R. O'Malley, L. Liu, C. Depcik, Comparative study of various cathodes for lithium ion batteries using an enhanced Peukert capacity model, *J. Power Sources* 396 (2018) 621–631.
- [26] S.H. Liu, X.L. Liu, R.F. Dou, W.N. Zhou, Z. Wen, L. Liu, Experimental and simulation study on thermal characteristics of 18,650 lithium-iron-phosphate battery with and without spot-welding tabs, *Appl. Therm. Eng.* (2020) 166.
- [27] A. Perea, A. Paoletta, J. Dube, D. Champagne, A. Mauger, K. Zaghbi, State of charge influence on thermal reactions and abuse tests in commercial lithium-ion cells, *J. Power Sources* 399 (2018) 392–397.
- [28] X.N. Feng, M.G. Ouyang, X. Liu, L.G. Lu, Y. Xia, X.M. He, Thermal runaway mechanism of lithium ion battery for electric vehicles: a review, *Energy Storage Mater.* 10 (2018) 246–267.
- [29] D.R. Conover, A.J. Crawford, V.V. Viswanathan, S. Ferreira, D. Schoenwald, Protocol for uniformly measuring and expressing the performance of energy storage systems, Richland, WA (United States), in: Pacific Northwest National Lab. (PNNL), 2014. Report No.: PNNL-22010 Rev. 1; Other: TE1400000 United States 10.2172/1136613 Other: TE1400000 PNNL English.
- [30] J.R. Belt, Battery Test Manual for Plug-In Hybrid Electric Vehicles, Idaho National Laboratory (INL), 2010. Report No.: INL/EXT-07-12536; TRN: US201022%83 United States 10.2172/991910 TRN: US201022%83 INL English.
- [31] S. Santhanagopalan, Q. Guo, P. Ramadass, R.E. White, Review of models for predicting the cycling performance of lithium ion batteries, *J. Power Sources* 156 (2) (2006) 620–628.
- [32] J. Newman, K.E. Thomas-Alyea, *Electrochemical Systems*, third ed., John Wiley & Sons, 2004.
- [33] G.L. Plett, *Battery Management Systems Volume 1 Battery Modeling*, Artech House, Norwood, MA, 2015.
- [34] M.J. Lain, J. Brandon, E. Kendrick, Design strategies for high power vs. High energy lithium ion cells, *Batteries* 5 (4) (2019).
- [35] K.A. Smith, C.D. Rahn, C.-Y. Wang, Control oriented 1D electrochemical model of lithium ion battery, *Energy Convers. Manag.* 48 (9) (2007) 2565–2578.
- [36] K.A. Smith, C.D. Rahn, C.-Y. Wang, Model order reduction of 1D diffusion systems via residue grouping, *J. Dyn. Syst. Meas. Contr.* 130 (1) (2008).
- [37] J. Landesfeind, J. Hattendorf, A. Ehl, W.A. Wall, H.A. Gasteiger, Tortuosity determination of battery electrodes and separators by impedance spectroscopy, *J. Electrochem. Soc.* 163 (7) (2016) A1373–A1387.
- [38] A.V. Randall, R.D. Perkins, X. Zhang, G.L. Plett, Controls oriented reduced order modeling of solid-electrolyte interphase layer growth, *J. Power Sources* 209 (2012) 282–288.
- [39] R. Deshpande, M. Verbrugge, Y.-T. Cheng, J. Wang, P. Liu, Battery cycle life prediction with coupled chemical degradation and fatigue mechanics, *J. Electrochem. Soc.* 159 (10) (2012) A1730–A1738.
- [40] J. Purewal, J. Wang, J. Graetz, S. Soukiazian, H. Tataria, M.W. Verbrugge, Degradation of lithium ion batteries employing graphite negatives and nickel-cobalt-manganese oxide + spinel manganese oxide positives: Part 2, chemical-mechanical degradation model, *J. Power Sources* 272 (2014) 1154–1161.
- [41] L. Liu, P. Guan, Phase-field modeling of solid electrolyte interphase (SEI) evolution: considering cracking and dissolution during battery cycling, *ECS Transact.* 89 (1) (2019) 101–111.
- [42] E.J. Seldin, Stress-strain Properties of polycrystalline graphites in tension and compression at room temperature, *Carbon* 4 (2) (1966) 177. -&.
- [43] V.V. Viswanathan, D. Choi, D. Wang, W. Xu, S. Towne, R.E. Williford, et al., Effect of entropy change of lithium intercalation in cathodes and anodes on Li-ion battery thermal management, *J. Power Sources* 195 (11) (2010) 3720–3729.
- [44] K.E. Thomas, J. Newman, Heats of mixing and of entropy in porous insertion electrodes, *J. Power Sources* 119–121 (2003) 844–849.
- [45] M. Guo, G. Sikha, R.E. White, Single-particle model for a lithium-ion cell: thermal behavior, *J. Electrochem. Soc.* 158 (2) (2011) A122–A132.
- [46] M. Safari, C. Delacourt, Mathematical modeling of lithium iron phosphate electrode: galvanostatic charge/discharge and path dependence, *J. Electrochem. Soc.* 158 (2) (2011) A63–A73.
- [47] S. Basu, R.S. Patil, S. Ramachandran, K.S. Hariharan, S.M. Kolake, T. Song, et al., Non-isothermal electrochemical model for lithium-ion cells with composite cathodes, *J. Power Sources* 283 (2015) 132–150.
- [48] M. Guo, R.E. White, A distributed thermal model for a Li-ion electrode plate pair, *J. Power Sources* 221 (2013) 334–344.
- [49] N. Takami, A. Satoh, M. Hara, T. Ohsaki, Structural and kinetic characterization of lithium intercalation into carbon anodes for secondary lithium batteries, *J. Electrochem. Soc.* 142 (2) (1995) 371–379.
- [50] M.W. Verbrugge, B.J. Koch, Electrochemical analysis of lithiated graphite anodes, *J. Electrochem. Soc.* 150 (3) (2003) A374–A384.
- [51] K. Kumaresan, G. Sikha, R.E. White, Thermal model for a Li-ion cell, *J. Electrochem. Soc.* 155 (2) (2008) A164–A171.
- [52] M. Doyle, J. Newman, A.S. Gozdz, C.N. Schmutz, J.M. Tarascon, Comparison of modeling predictions with experimental data from plastic lithium ion cells, *J. Electrochem. Soc.* 143 (6) (1996) 1890–1903.
- [53] L. Cai, R.E. White, Reduction of model order based on proper orthogonal decomposition for lithium-ion battery simulations, *J. Electrochem. Soc.* 156 (3) (2009) A154–A161.
- [54] M. Doyle, Y. Puentes, Computer simulations of a lithium-ion polymer battery and implications for higher capacity next-generation battery designs, *J. Electrochem. Soc.* 150 (6) (2003) A706–A713.
- [55] H. Zheng, J. Li, X. Song, G. Liu, V.S. Battaglia, A comprehensive understanding of electrode thickness effects on the electrochemical performances of Li-ion battery cathodes, *Electrochim. Acta* 71 (2012) 258–265.
- [56] C.-W. Wang, A.M. Sastry, Mesoscale modeling of a Li-ion polymer cell, *J. Electrochem. Soc.* 154 (11) (2007) A1035–A1047.
- [57] V.R. Subramanian, V. Boovaragavan, V. Ramadesigan, M. Arabandi, Mathematical model reformulation for lithium-ion battery simulations: galvanostatic boundary conditions, *J. Electrochem. Soc.* 156 (4) (2009) A260–A271.
- [58] L.O. Valøen, J.N. Reimers, Transport Properties of LiPF<sub>6</sub>-based Li-ion battery electrolytes, *J. Electrochem. Soc.* 152 (5) (2005) A882–A891.
- [59] R. Koerber, W.B. Zhang, L. de Biasi, S. Schweidler, A.O. Kondrakov, S. Kolling, et al., Chemo-mechanical expansion of lithium electrode materials - on the route to mechanically optimized all-solid-state batteries, *Energy Environ. Sci.* 11 (8) (2018) 2142–2158.
- [60] J.A. Nelder, R. Mead, A simplex-method for function minimization, *Comput. J.* 7 (4) (1965) 308–313.